



# W E S E

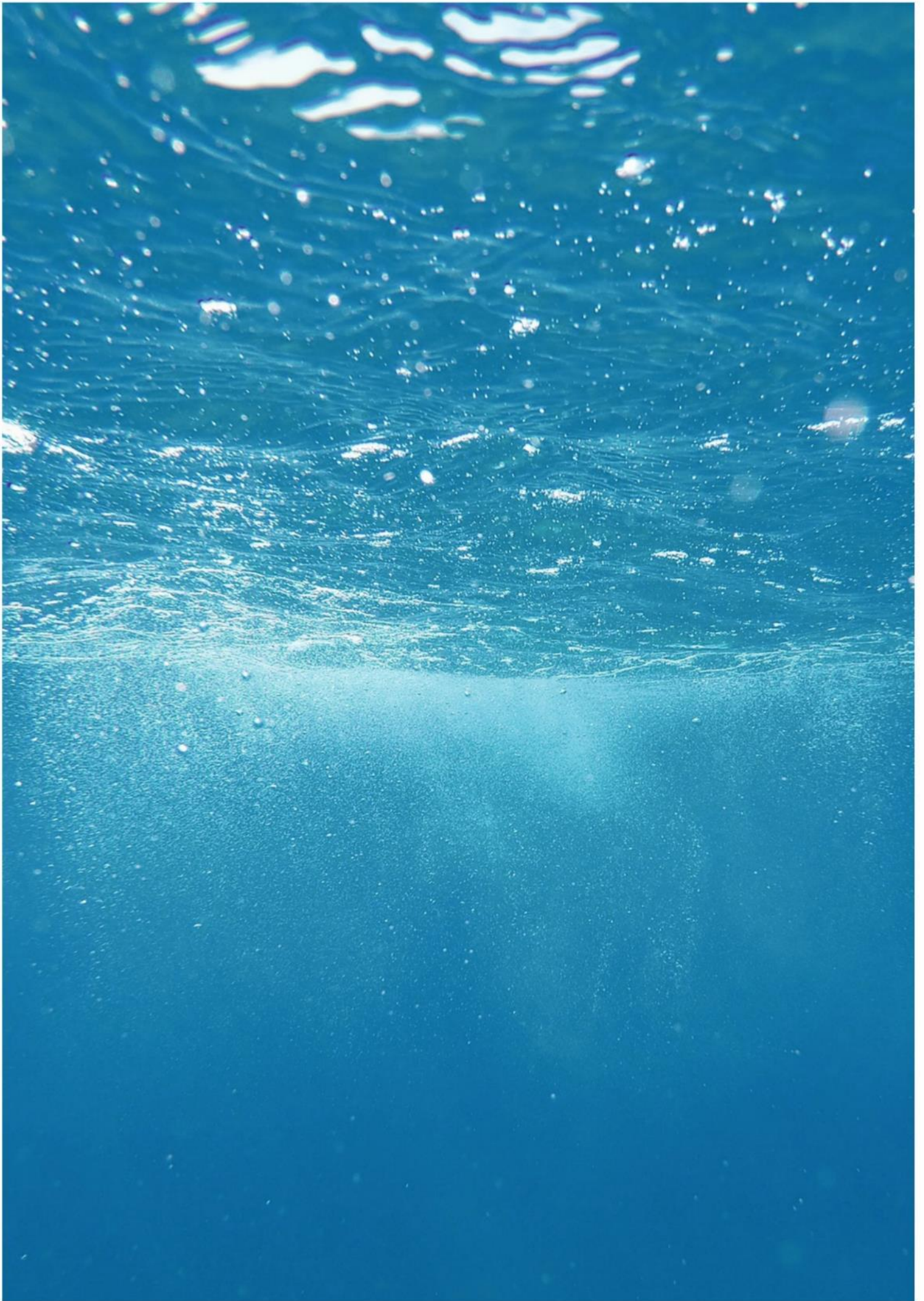
WAVE ENERGY  
IN SOUTHERN EUROPE

## DELIVERABLE 3.2 Acoustic Modelling



*This project has been funded by the European Commission under the European Maritime and Fisheries Fund (EMFF), Call for Proposals EASME/EMFF/2017/1.2.1.1 – “Environmental monitoring of wave and tidal devices”. This communication reflects only the author’s view. EASME is not responsible for any use that may be made of the information it contains.*





**WP 3**  
Deliverable 3.2 (Acoustic Modelling)

**PROJECT COORDINATOR**  
AZTI

**TASK LEADER**  
CTN

**AUTHORS**  
Ivan Felis (CTN)  
Eduardo Madrid (CTN)  
Juan Bald (AZTI)

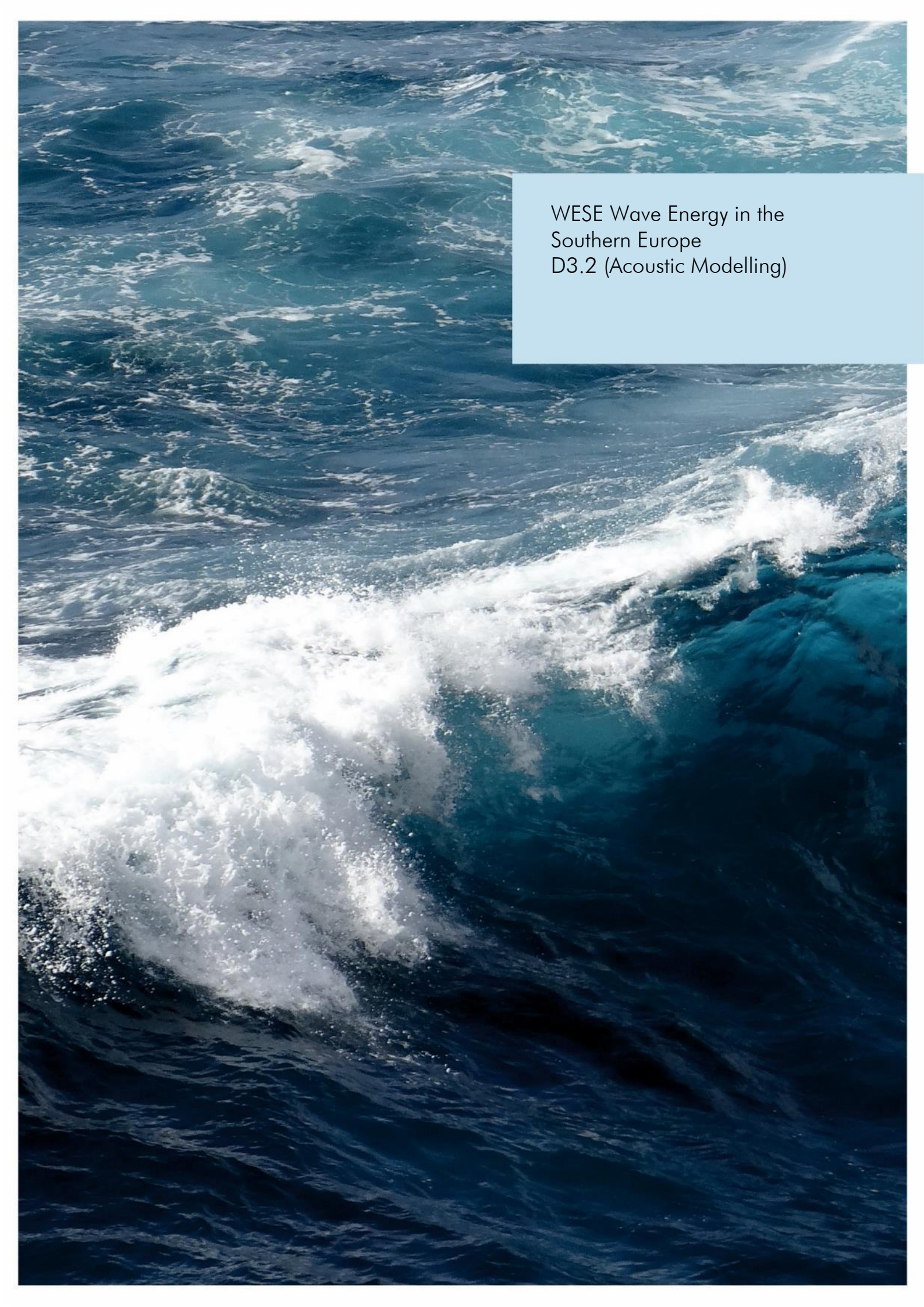
**SUBMISSION DATE**  
15 | May | 2021

**CITATION**

Felis, I., Madrid, E., Bald, J., 2021. Deliverable 3.2 Acoustic Modelling. Corporate deliverable of the WESE Project funded by the European Commission. Agreement number EASME/EMFF/2017/1.2.1.1/02/SI2.787640. 57 pp.



This project has been funded by the European Commission under the European Maritime and Fisheries Fund (EMFF), Call for Proposals EASME/EMFF/2017/1.2.1.1 – “Environmental monitoring of wave and tidal devices”. This communication reflects only the author’s view. EASME is not responsible for any use that may be made of the information it contains.

An aerial photograph of the ocean showing a prominent white wake from a boat cutting through the dark blue water. The wake consists of a series of white, frothy waves trailing behind the vessel. The surrounding water is a deep, textured blue with smaller, white-capped waves scattered across the surface. The overall scene is dynamic and captures the energy of the sea.

WESE Wave Energy in the  
Southern Europe  
D3.2 (Acoustic Modelling)

# CONTENTS

<b>1.</b>	<b>WESE PROJECT SYNOPSIS .....</b>	<b>7</b>
<b>2.</b>	<b>EXECUTIVE SUMMARY .....</b>	<b>9</b>
<b>3.</b>	<b>INTRODUCTION.....</b>	<b>10</b>
<b>4.</b>	<b>DATA AND METHODS .....</b>	<b>11</b>
4.1	ACOUSTIC PROPAGATION MODELS.....	11
4.2	ENVIRONMENTAL DATA .....	12
4.2.1	<i>Sound Speed Profile</i> .....	12
4.2.1.1	MARMOK-A-5.....	13
4.2.1.2	Mutriku .....	14
4.2.2	<i>Bathymetry</i> .....	14
4.2.2.1	MARMOK-A-5.....	15
4.2.2.2	Mutriku .....	16
4.2.3	<i>Seabed geo-acoustic properties</i> .....	16
4.2.3.1	MARMOK-A-5.....	17
4.2.3.2	Mutriku .....	18
4.3	SIMULATION PARAMETERS .....	19
4.3.1	<i>Source position</i> .....	19
4.3.2	<i>Hydrophone position</i> .....	20
4.4	SOURCE LEVELS.....	20
4.4.1	MARMOK-A-5.....	21
4.4.2	Mutriku.....	22
4.5	METHODOLOGY.....	23
<b>5.</b>	<b>RESULTS.....</b>	<b>24</b>
5.1	TRANSMISSION LOSSES .....	24
5.1.1	MARMOK-A-5.....	24
5.1.1.1	Fit to a geometric spreading loss model.....	27
5.1.2	Mutriku.....	29
5.1.2.1	Fit to geometric spreading losses model.....	32
5.2	SOURCE LEVELS.....	33
5.2.1	MARMOK-A-5.....	34
5.2.2	Mutriku.....	34
5.3	SOUND PRESSURE LEVELS.....	35
5.3.1	MARMOK-A-5.....	35
5.3.1.1	Sound maps .....	35
5.3.1.2	Metrics.....	41
5.3.1.3	Multiple sources.....	44
5.3.2	Mutriku.....	47

5.3.2.1 Sound maps .....	47
5.3.2.2 Metrics.....	52
<b>6. CONCLUSIONS.....</b>	<b>55</b>
<b>7. REFERENCES.....</b>	<b>56</b>

## 1. WESE project synopsis

The Atlantic seaboard offers a vast marine renewable energy (MRE) resource which is still far from being exploited. These resources include offshore wind, wave and tidal. This industrial activity holds considerable potential for enhancing the diversity of energy sources, reducing greenhouse gas emissions, and stimulating and diversifying the economies of coastal communities. Therefore, the ocean energy development is one of the main pillars of the EU Blue Growth strategy. While the technological development of devices is growing fast, their potential environmental effects are not well-known. In a new industry like MRE, and Wave Energy (WE) in particular, there may be interactions between devices and marine organisms or habitats that regulators or stakeholders perceive as risky. In many instances, this perception of risk is due to the high degree of uncertainty that results from a paucity of data collected in the ocean. However, the possibility of real risk to marine organisms or habitats cannot be ignored; the lack of data continues to confound our ability to differentiate between real and perceived risks. Due to the present and future demand for marine resources and space, human activities in the marine environment are expected to increase, which will produce higher pressures on marine ecosystems, as well as competition and conflicts among marine users. This context still continues to present challenges to permitting/consenting of commercial-scale development. Time-consuming procedures linked to uncertainty about project environmental impacts, the need to consult with numerous stakeholders and potential conflicts with other marine users appear to be the main obstacles to consenting WE projects. These are considered as non-technological barriers that could hinder the future development of WE in EU and Spain and Portugal in particular were, for instance, consenting approaches remain fragmented and sequential. Consequently, and in accordance with the Ocean Energy Strategic Roadmap published in November 2016<sup>1</sup>, the main aim of the project consists on overcoming these non-technological barriers through the following specific objectives:

- Development of environmental monitoring around wave energy converters (WECs) operating at sea, to analyse, share and improve the knowledge of the positive and negative environmental pressures and impacts of these technologies and consequently a better knowledge of real risks.
- The resulting data collection will be used to apply and improve existing modelling tools and contribute to the overall understanding of potential cumulative pressures and impacts of larger scale, and future, wave energy deployments.

- Development of efficient guidance for planning and consenting procedures in Spain and Portugal for WE projects, to better inform decision-makers and managers on environmental real risks and reduce environmental consenting uncertainty of ocean WE introducing the Risk Based Approach suggested by the RiCORE, a Horizon 2020 project, which underline the difficulties for developers with an existing fragmented and sequential consenting approaches in these countries;
- Development and implementation of innovative maritime spatial planning (MSP) Decision Support Tools (DSTs) for Portugal and Spain for site selection of WE projects. The final objective of such tools will be the identification and selection of suitable areas for WE development, as well as to support decision makers and developers during the licensing process. These DSTs will consider previous findings (both environmental and legal, found in RiCORE) and the new knowledge acquired in WESE in order to support the development of the risk-based approach mentioned in iii);
- Development of a Data Sharing Platform that will serve data providers, developers and regulators. This includes the partners of the project. WESE Data Platform will be made of a number of ICT services in order to have: (i) a single web access point to relevant data (either produced within the project or by others); (ii) Generation of OGC compliant requests to access data via command line (advanced users); (iii) a dedicated cloud server to store frequently used data or data that may not fit in existing Data Portals; (iv) synchronized biological data and environmental parameters in order to feed models automatically.

## 2. Executive summary

In the WESE project scope, Work Package 3 aims to model electromagnetic and acoustic fields, as well as marine dynamics, in sites where Wave Energy Converters (WEC) are operating in real sea conditions in Spanish and Portuguese coastal waters, representing different types of technology, sites and, therefore, types of marine environments (onshore, nearshore and offshore) that can potentially be affected by wave energy projects: (i) Idom-Oceantec MARMOK-A-5, installed in the Biscay Marine Energy Platform (BiMEP) in Spain; (ii) Mutriku Wave Power Plant, in operation in the Mutriku (Spain); and (iii) WaveRoller (AW-Energy), installed in Peniche (Portugal).

This specific deliverable (3.2) aims to model the underwater acoustic fields radiated by the wave energy converters with the support of the results of the deliverable D2.3. To achieve this goal, a parabolic equation acoustic propagation model with full range dependence in environment variables (bathymetry, temperature, salinity, and seabed substrate elastic parameters) has been implemented for three different frequencies (62.5, 125, and 1000 Hz), several depth levels, ranging from 5 meters to 100 meters, and different sea states (characterized by significant wave height).

### 3. Introduction

Noise is defined according to the Marine Strategy Framework Directive (MSFD) as an “anthropogenic sound that has the potential to cause negative impacts on the marine environment, including component biota but not necessarily the whole environment”. It is considered one of the main impacts of marine renewable energy converters operation [1], given the acute importance of sound for marine life, especially for cetaceans [2].

Given the necessary uprising of renewable energy technologies, in which marine energy promises (despite being still in testing phase of development) to be a solid support to already more established technologies (photovoltaic, wind), a good understanding of the impacts associated to these technologies must be achieved [3] [4]. WESE focuses on one of the main types of marine energy technology: Wave Energy Converters (WEC); that is, devices that obtain energy from the movement of sea waves.

In this deliverable we present the work carried out in the acoustic modelling for the three energy converters studied in the WESE project: MARMOK-A-5 (offshore oscillating water column WEC), Mutriku (onshore oscillating water column WEC), and WaveRoller, (off-shore surge WEC). Note that, even if they all need waves to operate, WaveRoller exploits the horizontal movement of mass waters (produced in shallow water) as a consequence of waves dynamics, while MARMOK-A-5 and Mutriku ultimately rely on the vertical movement of the sea surface to produce energy. A more detailed description of each device can be found in other deliverables, such as D2.1 [5].

Having already analysed the acoustic measurements carried out in the monitoring campaigns described in D2.1 and D2.3 [6], the next step is modelling the acoustic fields in the area surrounding the WECs. Noise modelling can be a useful tool to assess underwater noise, as indeed is suggested by the TG-Noise (EU Technical Group on underwater noise), the combined use of underwater noise measurements and modelling is the most effective way to monitor ambient noise levels and trends in the seas [7].

## 4. Data and methods

We present a briefly introduction of the acoustic propagation numerical models used in this study, as well as the different sources of inputs data for implementing them.

### 4.1 Acoustic propagation models

The spatiotemporal propagation of an acoustic wave is usually described by the acoustic linear wave equation<sup>1</sup>:

$$\nabla^2 p(\vec{r}, t) - \frac{1}{c^2} \frac{\partial^2 p(\vec{r}, t)}{\partial t^2} = 0 \quad (1)$$

where  $p(\vec{r}, t)$  is the acoustic pressure at position  $\vec{r}$  and time  $t$ , and  $c$  is the sound speed in the medium.

Solving this equation directly with arbitrary boundary conditions is computationally intensive (e.g., finite difference/elements methods), so that some approximations are mandatory. Three of these approximations stand out: ray theory, normal modes, and parabolic equation approximation. They are suited for different conditions respect to the frequency under study, the sea depth, and the range dependence [8]. Ray theory models are usually best suited for high frequencies, while normal modes and parabolic equation models are more efficient for low frequencies. In this study a parabolic equation model was chosen.

Additionally, there are other kind of models much more simplistic, that we shall denote analytic models. These usually ignore some (if not all) of the environmental data, allowing much faster calculations. Among these, we remark here the spreading loss model, in which the transmission losses are described solely as a function of distance as:

$$TL(r) = a \log(r/r_{1m}) \quad [\text{dB re 1 m}] \quad (2)$$

where  $r$  is the radial distance from the source,  $r_{1m}$  is the reference distance (1 meter), and  $a$  is a coefficient that characterizes the spreading of wavefronts, typically between 20 (pure spherical propagation) and 10 (cylindrical wavefront propagation).

While  $TL$  is the main output of an acoustic propagation model, to obtain levels referenced to a certain source, they must be converted to sound pressure levels (SPL), for which the acoustic source level (SL) must be known. More details about this conversion can be found in section 4.4.

---

<sup>1</sup> More specifically, the typical acoustic propagation models are based on approximations of the wave equation in frequency space (the so called Helmholtz equation).

## 4.2 Environmental data

Detailed propagation models take into account data about the bathymetry, sound speed profile, and seabed composition of the environment. These environmental parameters influence the transmission of underwater acoustic waves by different mechanisms, as is briefly explained in the following sections. In what follows, it is assumed that the data have all been interpolated to a common regular grid (the same in which the definitive noise maps will be eventually calculated) with a cell size of approximately 100 meters.

The coordinate system used in this study is the Universal Transversal Mercator (UTM) projected coordinate system, specified in the considered zones: for MARMOK-A-5 and Mutriku it corresponds to the zone 30T, while for the WaveRoller site (Peniche, Portugal), it is the zone 29S; this projected coordinate system minimizes distortions within each zone.

### 4.2.1 Sound Speed Profile

The sound speed profile (SSP) describes the dependence of sound speed with respect to water depth and influences the path of propagation of the wavefronts by means of the refraction phenomenon. Because sound speed in the ocean depends mainly on temperature, pressure (or equivalently, depth) and salinity, these three variables define the sound speed profile in the water column. Naturally, the sound speed profile in a particular point is not constant in time; although the depth may vary in a daily basis (surges), and salinity may vary drastically in some particular locations, it is the temperature the most relevant parameter in the temporal characterization of SSPs. In this context, SSPs usually show seasonal dependence, as can be shown in Figure 1. It is most relevant in deep waters, in which boundary reflections are not very relevant for long range propagation.

For this deliverable, the Copernicus database<sup>2</sup> was used to obtain temperature and salinity fields in depth for the considered spatiotemporal domains: in particular, the GLOBAL\_ANALYSIS\_FORECAST\_PHY\_001\_024 dataset was used, with a spatial resolution of 1/12 degree and a temporal resolution of a month (although only data corresponding to the time period of the mobile monitoring was eventually used). From these data, the sound speed in the water column is readily calculated and interpolated to the common grid of 100 m resolution, using the Mackenzie model for speed of

---

<sup>2</sup> Link to site: <https://marine.copernicus.eu/>

sound in the ocean [9]. This will allow us to sample the SSP in every point of the grid to improve the model accuracy.

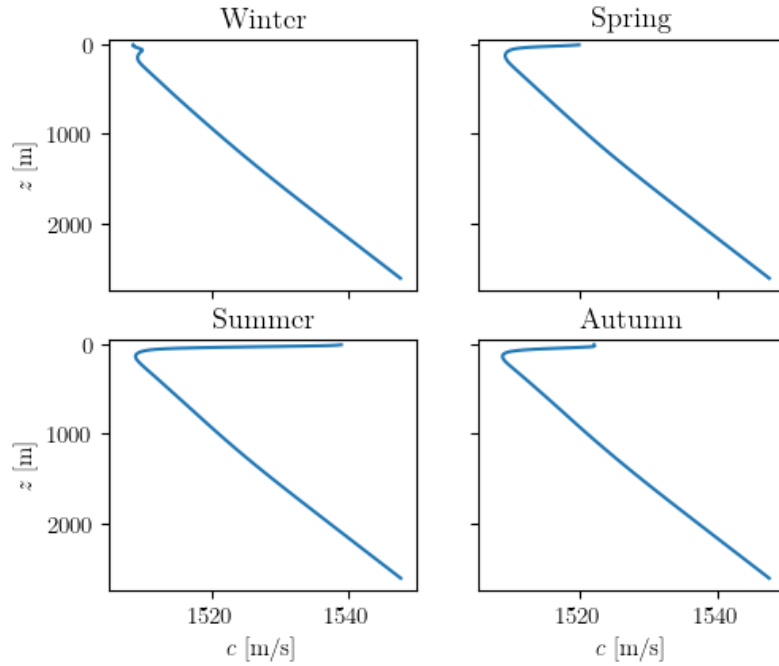


**Figure 1.** Example of seasonal dependence of real sound speed profiles calculated in the Western Mediterranean (specifically, south-eastern coast of Spain).

#### 4.2.1.1 MARMOK-A-5

Since the temporal acoustic monitorization was undertaken in May 2019, mean temperature and salinity data for this month was used to calculate the SSP in the grid. As a means of illustration, the sound speed for  $z = 5$  m is displayed in Figure 2, as well as the average SSP (for the whole region). A SOFAR channel is found at around 110 m depth, although the variability in sound speed is not greater than 7 m/s.

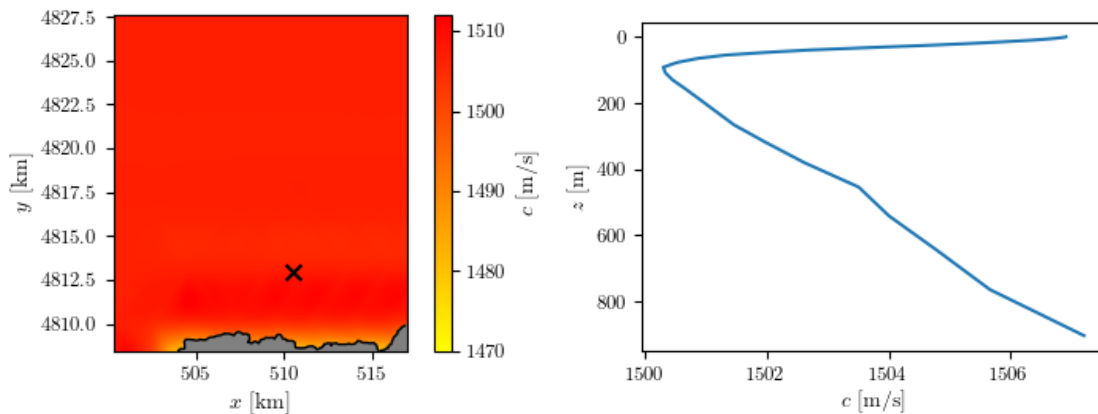


**Figure 2.** Left: spatial dependence of SSP in the polar plane for MARMOK-A-5. Right: mean SSP. Device is marked as black cross.

#### 4.2.1.2 Mutriku

Given the proximity between the BiMEP test site and the Mutriku power plant, and the fact that the acoustic monitoring was carried out in the same month, we expect to find very similar sound speed profiles. In fact, as can be seen in Figure 3, the (spatially) averaged sound speed profile is very similar to that of the previous case, considering only the matching depths. The beginnings of a SOFAR channel can be guessed at the 100-meter depth level, as was expected from the BiMEP site mean SSP.

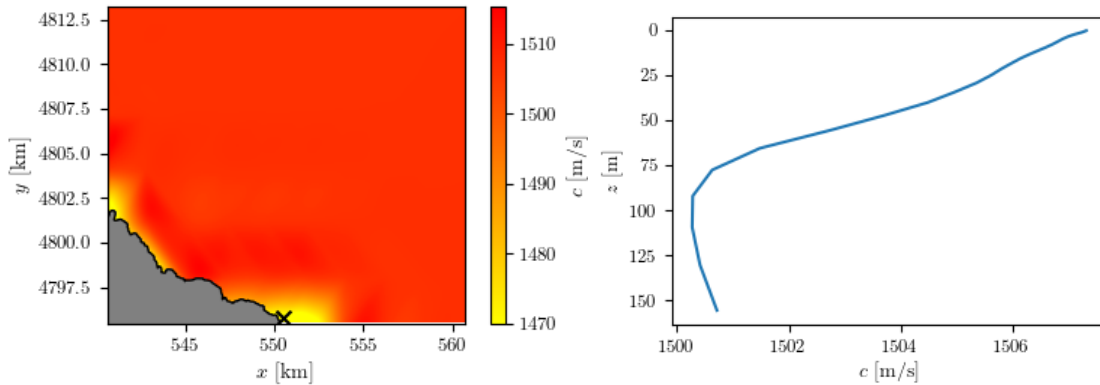


**Figure 3.** Left: spatial dependence of SSP in the polar plane for the scenario of Mutriku. Right: mean SSP. Device is marked as black cross.

#### 4.2.2 Bathymetry

The bathymetry, together with the sea surface, are essentially the only boundaries that the acoustic waves meet in their propagation. The sea surface is usually modelled as a pressure release surface (vacuum), which is a very good approximation, considering the great difference of acoustic impedance of air and water. The seabed, spatially characterized by its bathymetric profile, is a more complex media altogether.

The bathymetry influences how the acoustic waves are reflected, and therefore, influences the distribution of transmission losses along their course, as is explicitly shown in the simulations of **Figure 4**. It is particularly important in shallow water environments, as those encountered in this project. In fact, shallow water channels work as a low frequency filter with the cut-off frequency approximately given by the expression:

$$f_c = \frac{c_1}{4z} \sqrt{\frac{1}{1 - (c_1/c_2)^2}} \quad (3)$$

where  $c_1$  and  $c_2$  are the sound speed in water and sound speed in the seabed, respectively. This phenomenon will be seen in all simulations, especially for the lowest frequency, that is, 62.5 Hz.

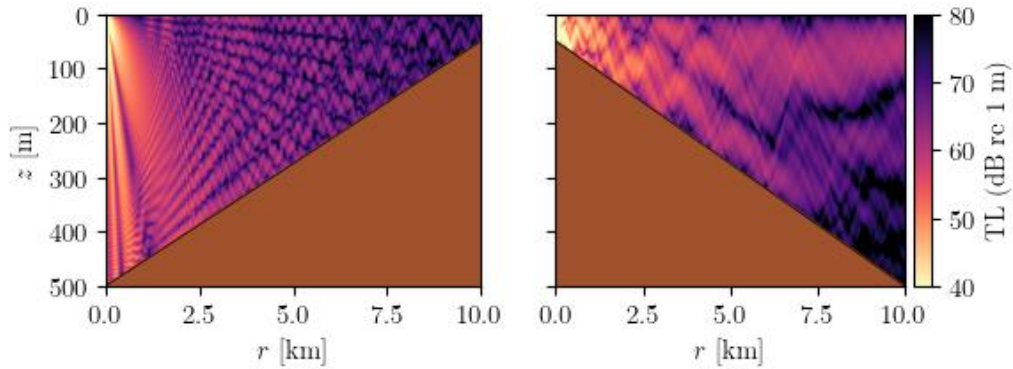


**Figure 4.** Effect of bathymetry on TL, simulated by a parabolic equation model for a source depth of 20 meters and frequency of 100 Hz.

All bathymetries of this study were obtained from the EMODnet bathymetry service<sup>3</sup>. It has a spatial resolution of 0.001 decimal degrees, that is equivalent to about 80 meters of distance for the typical latitudes in this study.

#### 4.2.2.1 MARMOK-A-5

The BiMEP test site is characterized by shallow waters that are more or less constant (around 100 m depth) up until the parallel defined by 4825 km in the y-coordinate (Figure 5). There, an abrupt decline appears, surpassing the 1000 m depth level. In more detail, the average depth is 149.6 m, the maximum is 1112.6 m, while the standard deviation is about 177 m. The prevalence of shallow water means that low frequencies will be transmitted very poorly, because of the cut-off filter effect stated in the previous section.

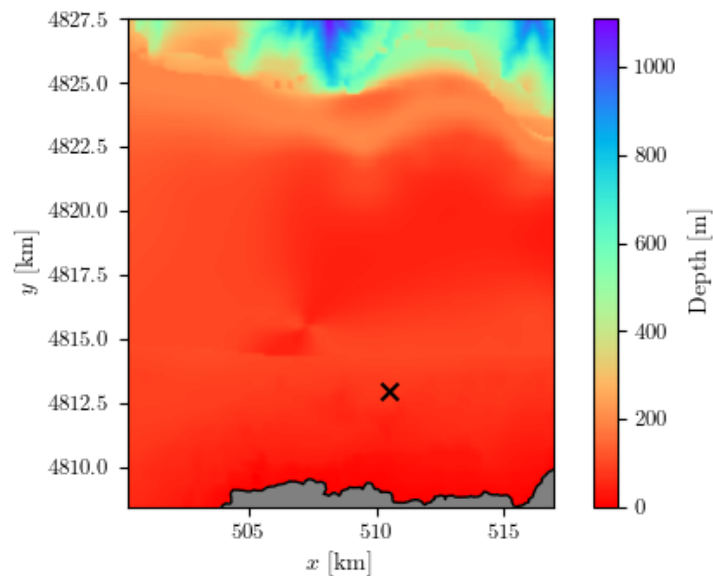


**Figure 5.** Bathymetry of the region around the MARMOK-A-5 converter (marked with a black a cross).

<sup>3</sup> Link: <https://portal.emodnet-bathymetry.eu/#>.

#### 4.2.2.2 Mutriku

The bathymetry of the Mutriku shores is even shallower than for MARMOK-A-5, as can be seen in Figure 6 (note the different values in the colour scale range), with a maximum depth of 155.8 m and an average depth of 86.9 m, with a standard deviation of 65.7 m. Therefore, the same filtering phenomena will appear in the propagation calculations, if not stronger than for the MARMOK-A-5 environment.

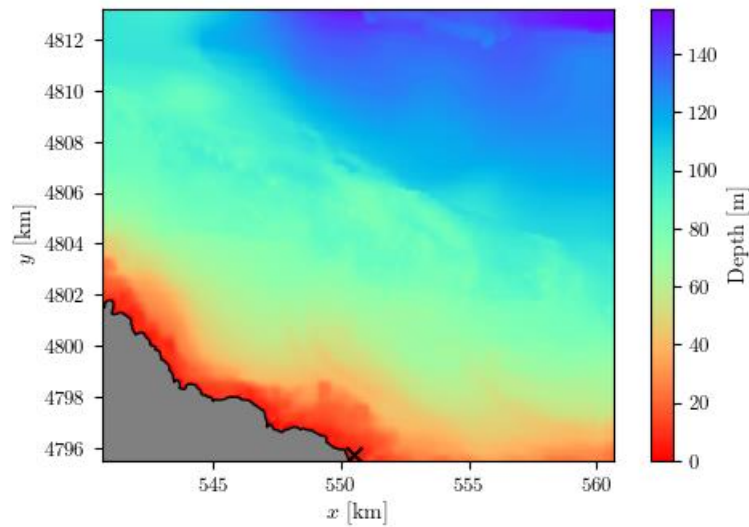


**Figure 6.** Bathymetry of the region around the Mutriku power plant (marked with a black cross).

#### 4.2.3 Seabed geo-acoustic properties

We will refer as seabed geo-acoustic properties to density, sound speed and acoustic sound attenuation of transversal and longitudinal waves (denoted as  $\rho$ ,  $c_T$ ,  $c_L$ ,  $a_T$ ,  $a_L$ , respectively) specifically.

These five parameters characterize the transmission, reflection, and absorption of acoustic waves in the water-substrate boundary, and thus are crucial to obtain correct acoustic energy levels in the water channel (Figure 7). Therefore, they are particularly essential in shallow water environments, in which reflections play a big role in acoustic transmission. For this reason, it is important to sample them as best as is possible, given the particularly shallow waters of all sites.

Available seabed data usually consists of qualitative information regarding the type of seabed substrate. These types of sediments must be associated with their corresponding geo-acoustic parameters mentioned before to be of any use to the models. In general, converting this (qualitative) type of information to (quantitative) numerical data is not straightforward. In this regard, we compared with the existent literature to find equivalent categories of sediment for which geo-acoustical

parameters have been experimentally measured [10, 11]. Table 1 shows the geo-acoustic parameters corresponding to the identified seabed substrates for any of the study scenarios.

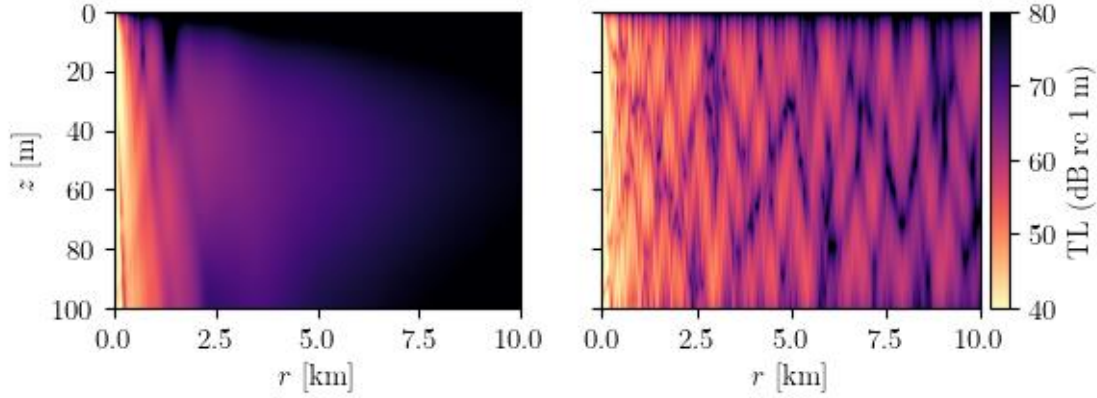


**Figure 7.** Effect of seabed geo-acoustic properties on the transmission losses in the acoustic duct for a source in 20 m and 100 Hz of frequency. Left:  $\rho = 1.5 \text{ g/cm}^3$ ,  $c_L = 1515 \text{ m/s}$ ,  $a_L = 0.15 \text{ dB } \lambda^{-1}$ . Right:  $\rho = 2 \text{ g/cm}^3$ ,  $c_L = 1800 \text{ m/s}$ ,  $a_L = 0.9 \text{ dB } \lambda^{-1}$ .

**Table 1.** Seabed classes and their geo-acoustic properties for the MARMOK-A-5 case.

Category	$\rho \text{ [g/cm}^3\text{]}$	$c_L \text{ [m/s]}$	$c_T \text{ [m/s]}$	$a_L \text{ [dB/\lambda]}$	$a_T \text{ [dB/\lambda]}$
Mixed sediments	1,6	1560	0	0,2	0
Sandy mud	1,7	1605	0	1,0	0
Muddy sand	1,8	1650	0	1,1	0
Fine sand	1,9	1680	0	1,0	0
Coarse sand / Mixed	2,0	1800	0	0,9	0
Rock	2,6	4750	2350	0,1	0,2

In the following sections, these properties are specified for each case. They have been extracted from different data sources that shall be specified, and all are shapefiles (vector data) that have been rasterized to a grid to easily make the proper interpolants to use in the acoustic propagation models. Furthermore, in case of missing data (gaps), these were filled in with the most prevalent seabed substrate of the particular dataset.

#### 4.2.3.1 MARMOK-A-5

For the BiMEP test site, we used a shapefile from the cartography repository of the Basque Country administration<sup>4</sup> with information about type of sediment. Most of the seabed area consisted of sedimentary-like substrate. We should also note that some

<sup>4</sup> Link to site: <https://www.geo.euskadi.eus/s69-15375/es/>

areas of our spatial grid are uncovered by this dataset; in these cases, it was assumed that the bottom was of the same type as the most prevalent one in the area.

As is clear, the most common seabed substrate is composed of muddy sand for this area, with rocky outcrops near the shore. Nonetheless, much part of this region was missing data, that is why the north region is so homogeneous in muddy sand.

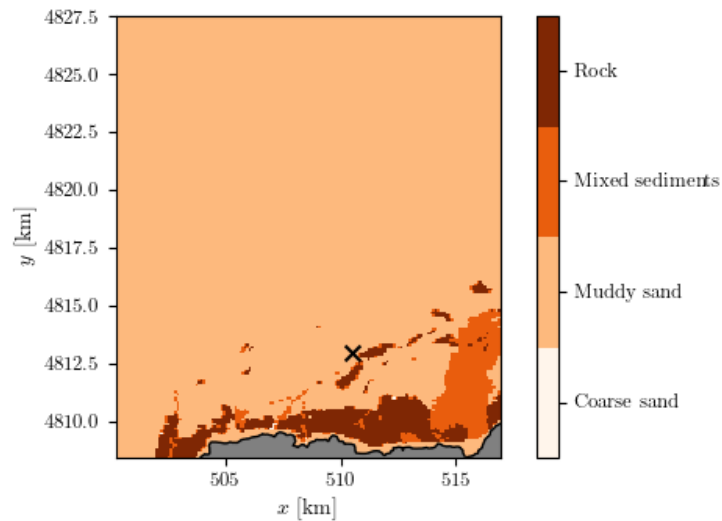


**Figure 8.** Types of seabed substrate in the region around Mutriku power plant (marked with a cross).

#### 4.2.3.2 Mutriku

In the case of Mutriku, the same database (shapefile from the Basque administration) used for MARMOK-A-5 is used since it covers all Basque waters. In this context, we find very similar types of seabed substrate, due to their relative proximity. They are shown in **Figure 9**, where the prevalence of coarse sand and mixed sediments is noticeable.

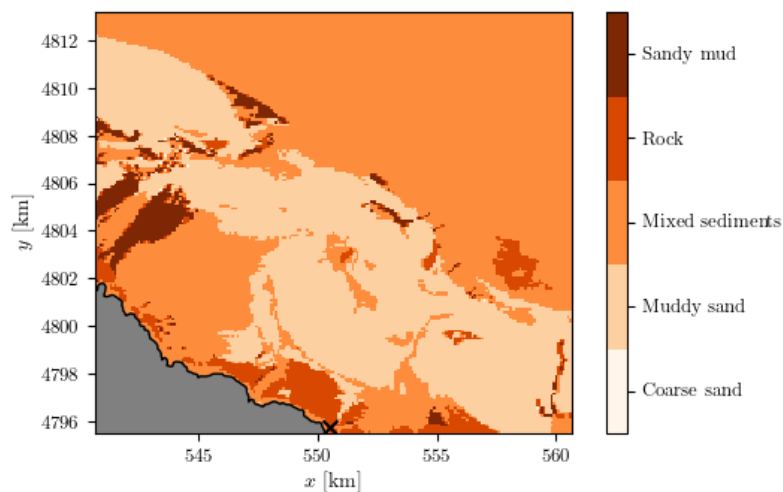


**Figure 9.** Types of seabed substrate in the region around Mutriku power plant (marked as a cross).

### 4.3 Simulation parameters

In this section we specify the values of some parameters more related to the mathematical aspects of simulations *per se*. Without any specific order, these are:

- The transect resolution (e.g., distances at which the environmental data are sampled along the transect) will be set to 50 meters. However, for the longest transects, this value will be adapted to higher values because of numerical limitations. In the other hand, for very short transects, this distance will be iteratively halved until at least 20 samples can be taken for a given transect. The transect coordinates are calculated considering the curvature of the Earth, that is, transects are actually geodesics.
- The distance between receptors (points at which the model samples results) will be of 20 meters in radial distance whereas for depth receivers it will be of 0.5 m (these must not be confused with the points at which the model performs the calculations – these are automatically calculated by the program itself depending on the frequency).
- Regarding the sound speed profile, it will be sampled from 2 up to 5 meters (depending on the maximum depth along the transect).
- Acoustic absorption has been considered in the model (although it is mostly irrelevant for the selected frequencies).

In any case, at the end of the simulations (for each device) all these results will be accordingly interpolated to the aforementioned common grid, a regular grid of 100 m distance between adjacent cells, for the depths contained in the following list: 5, 10, 20, 30, 40, 50, 60, 70, 80, 90, 100.

#### 4.3.1 Source position

All sources will be considered a point (acoustic monopole). While this may seem unrealistic, and indeed is, for long propagation ranges (e.g., where far-field conditions are met) it is a fairly good approximation. The coordinates of such equivalent point sources are shown in Table 2. In case of the MARMOK-A-5 device, source depth was calculated as the depth at which the centre of the device was located, assuming the moving parts of the converters would transmit the vibration through the metallic hull. As for Mutriku, since there is no significant expected coupling between the moving parts (turbines) and the concrete wall that is partially submerged in water, the source was placed as close to the sea surface as possible.

**Table 2.** Acoustic monopole.

WEC	Latitude [°N]	Longitude [°E]	Depth [m]
MARMOK-A-5	43.4695	-2.8698	20
Mutriku	43.3126	-2.3771	1

### 4.3.2 Hydrophone position

As is explained the following section, it is necessary to backpropagate the results from the models to obtain the levels at 1 meter from the source. In the Table 3, the exact coordinates of the location of the hydrophones are shown.

**Table 3.** Coordinates of the hydrophones location.

WEC	Latitude [°N]	Longitude [°E]	Depth [m]
MARMOK-A-5	43.46997	-2.86908	70
Mutriku	43.31947	-2.36903	10

## 4.4 Source levels

Source level is defined as the SPL at one meter of distance from the equivalent source acoustic monopole and is denoted by SL. This variable can be calculated using the results of deliverable D2.3 (Acoustic Monitoring) in addition to propagation modelling, that is, SPL values for all frequency bands centred in thirds of octave from 10 Hz to 10 kHz and different sea states (significant wave height).

In more detail, we obtained sound pressure levels associated to the background (e.g., device not working) and to the operation of the converters (working), henceforth denoted as  $SPL_{off}$  and  $SPL_{on}$ . For those cases in which  $SPL_{on} > SPL_{off}$ , we identify the source level by simply adding

$$SL = SPL_{on} + TL_0 \quad (4)$$

where  $TL_0$  denotes the propagation losses from the source to the hydrophone location. Therefore, to obtain the source level of a device an acoustic propagation model must be applied to the specific characteristics of the underwater acoustic channel connecting the device to the hydrophone in order to find out the value of  $TL_0$ .

Note that these values will actually impose an upper bound to the actual source level, as they ignore the background noise.

### 4.4.1 MARMOK-A-5

Recalling from the results of deliverable D2.3,  $SPL_{off}$  and  $SPL_{on}$  results for the three frequencies are attached in Table 4 and Table 5, respectively; recall that these values are averages. In general, the background noise levels are below those corresponding to the operation of the device, but it must be noted that the distance between hydrophone and converter was only approximately 90 meters.

**Table 4.**  $SPL_{off}$  values for MARMOK-A-5 [dB re 1  $\mu$ Pa].

$H_w$	$f$ [Hz]		
	62.5	125	1000
[0,1)	91.7	90.7	87.4
[1,2)	95.9	95.0	91.1
[2,5)	101.2	100.2	95.2

**Table 5.**  $SPL_{on}$  values for MARMOK-A-5 [dB re 1  $\mu$ Pa].

$H_w$	$f$ [Hz]		
	62.5	125	1000
[0,1)	101.3	93.2	88.3
[1,2)	104.2	95.2	91.2
[2,5)	105.4	98.3	96.8

In the Figure 10, the SPL values for the 1/3 octaves centred bands from 10 Hz to 10 kHz are displayed, for the aforementioned “off” and “on” states.

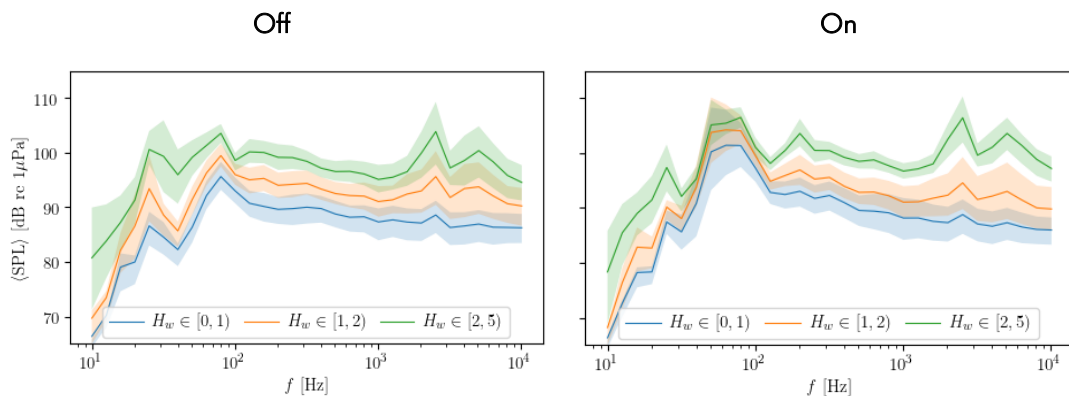


**Figure 10.** Mean SPL values for background signals classified in wave height bins for MARMOK-A-5. Deviations defined by Q1 (percentile 25) and Q2 (percentile 75) are added as shaded bands.

### 4.4.2 Mutriku

The average sound pressure levels for the frequencies and significant wave height bins for background noise and (background plus) converter noise is shown in Table 6 and Table 7. Recall that, as was concluded in D2.3, the Mutriku power plant did not show any significant noise with respect background levels, in the location of the fixed hydrophone.

**Table 6.** SPL<sub>off</sub> values for Mutriku [dB re 1 μPa].

$H_w$	$f$ [Hz]		
	62.5	127	1000
[0,1)	75.2	76.9	85.4
[1,2)	80.1	89.2	82.3
[2,5)	79.5	82.1	83.5

**Table 7.** SPL<sub>on</sub> values for Mutriku [dB re 1 μPa].

$H_w$	$f$ [Hz]		
	62.5	127	1000
[0,1)	77.4	79.1	81.4
[1,2)	79.3	80.7	82.9
[2,5)	82.5	83.9	85.2

In the Figure 11, the SPL values for the whole range of frequencies is displayed, for the “off” and “on” states. Note the relative similarity between values for the different conditions.

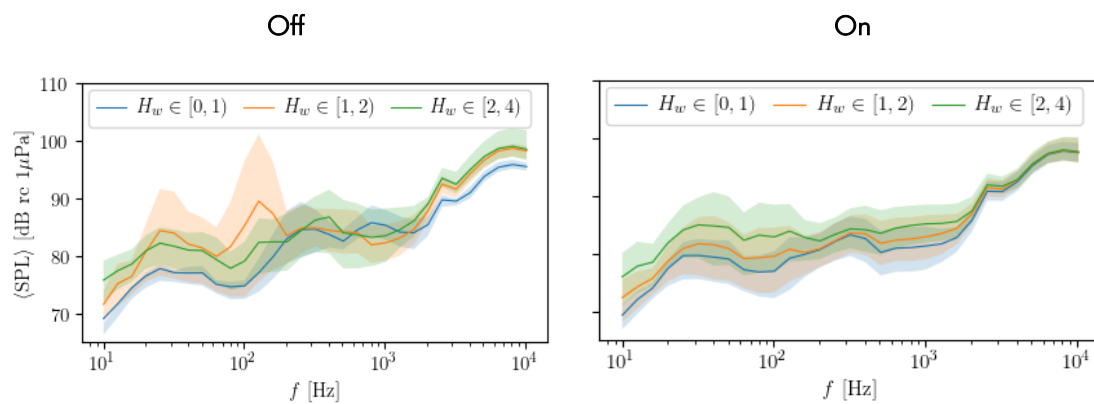


**Figure 11.** Mean SPL values for background signals classified in wave height bins in Mutriku. Deviations defined by Q1 (percentile 25) and Q2 (percentile 75) are added as shaded bands.

## 4.5 Methodology

For the calculation of transmission losses fields, a Nx2D approach was used. The chosen model was the Monterey-Miami Parabolic Equation (MMPE) model, which is a parabolic equation model able to take into account range dependency on sound speed profile, bathymetry, and seabed geo-acoustic properties [12]. This allows us to maximize the amount of information we can input the model. The workflow is all governed by Python scripts.

It is also expected to behave correctly in the mostly shallow water environments in which the WECs are located, as well as in the lower part of the frequency spectra. As a possible downside is the increasing computation costs for higher frequencies, which, fortunately, are not key in this study, in which a focus on the MSFD D11 frequencies has been favoured (63, 125 Hz).

The key steps of the methodology are:

1. Homogenize the environmental datasets (bathymetry, SSP, geo-acoustic properties) into a common spatial grid. Interpolation from the original data (usually georeferenced in geographic coordinates – latitude, longitude -) to this common grid is performed, after transforming the coordinates to the transversal Mercator projection (UTM) if necessary. This was already explained in section 4.2. For better computation efficiency, calculate and store the interpolants for every variable field.
2. Draw transects (geodesics) from the source up to the end of the grid, spanning the whole polar plane, and sample the environmental parameters along them (via the stored interpolants). Run the model for each frequency and transect (for the whole water column) and store in memory the resulting TL values as well as their corresponding spatial coordinates and depths. An angular resolution of 2 degrees was used.
3. Interpolate the unstructured TL data into the grid for each frequency and depth of interest; that way, readily transmission losses field is obtained for each case. Section 5.1 shows some results from this step.
4. Having obtained the SL values for all frequencies and wave heights (section 0), the definitive sound pressure level field caused by the device (denoted simply as SPL), are easily calculated as  $SPL = SL - TL$ . These will be the results from which posterior analysis will be carried out in order to extract useful metrics, as shown in lastly in section 5.3.

## 5. Results

A total of 99 transmission losses polar maps were calculated in total (11 depths, 3 frequencies and 3 devices). The studied depths are 5, 10, 20, ..., and so on up to 100 metres. From them another 297 maps were obtained, now with sound pressure level values, where the extra number of maps comes from adding another dimension to the study, which is the significant wave height, characterized as three bins, [0,1), [1,2), and [2,5) meters, in accordance with the performed analysis of deliverable 2.3 of this project.

### 5.1 Transmission losses

In this section the simulated TL fields are presented for every frequency and two selected depths (5 and 50 meters), by way of illustration. Additionally, maps for the averaged (in depth) TL field are also shown to further reduce the dimensionality of the results and check the global directivity of the source. These maps characterize how efficiently is sound transmitted at a given depth and frequency from the source position. In most of them the typical wave interference pattern can be distinguished, due to refraction and reflections with top and bottom boundaries of the ocean.

Note that for some depths, the corresponding horizontal planes in which TL fields are sampled will undoubtedly cut through the seabed, for that reason, the raw interpolated TL fields will be directly masked according to the bathymetry (as both share the same coordinates grid, i.e., the common grid), to avoid taking into account values of transmission losses in cells for which the sea depth is smaller than the depth of the horizontal plane in which the TL fields are calculated. In other words, only the values of TL in the water column are considered in the calculation of depth-averaged fields.

#### 5.1.1 MARMOK-A-5

First, we present the transmission losses along two different and non-consecutive transects (recall that the Nx2D method involves iterating through transects) for the three considered frequencies in this task. These plots show information about the whole water column, but only in one direction each. In Figure 12 we can see these transects drawn on the map, in which the bathymetry is also shown, while in Figure 13 the corresponding transmission losses plots are presented.

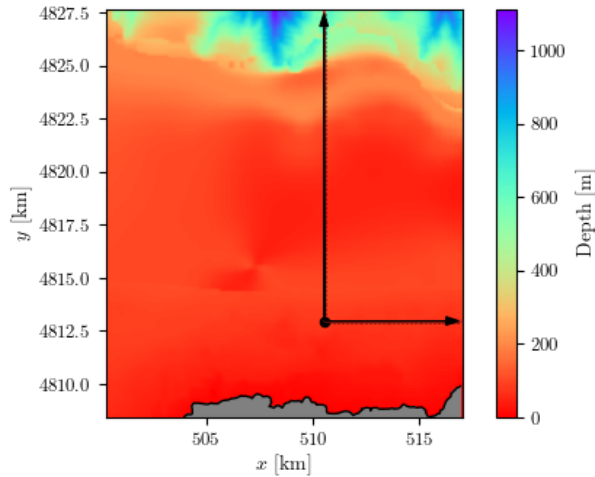


Figure 12. Samples of simulated TL along transects in the MARMOK A-5 scenario.

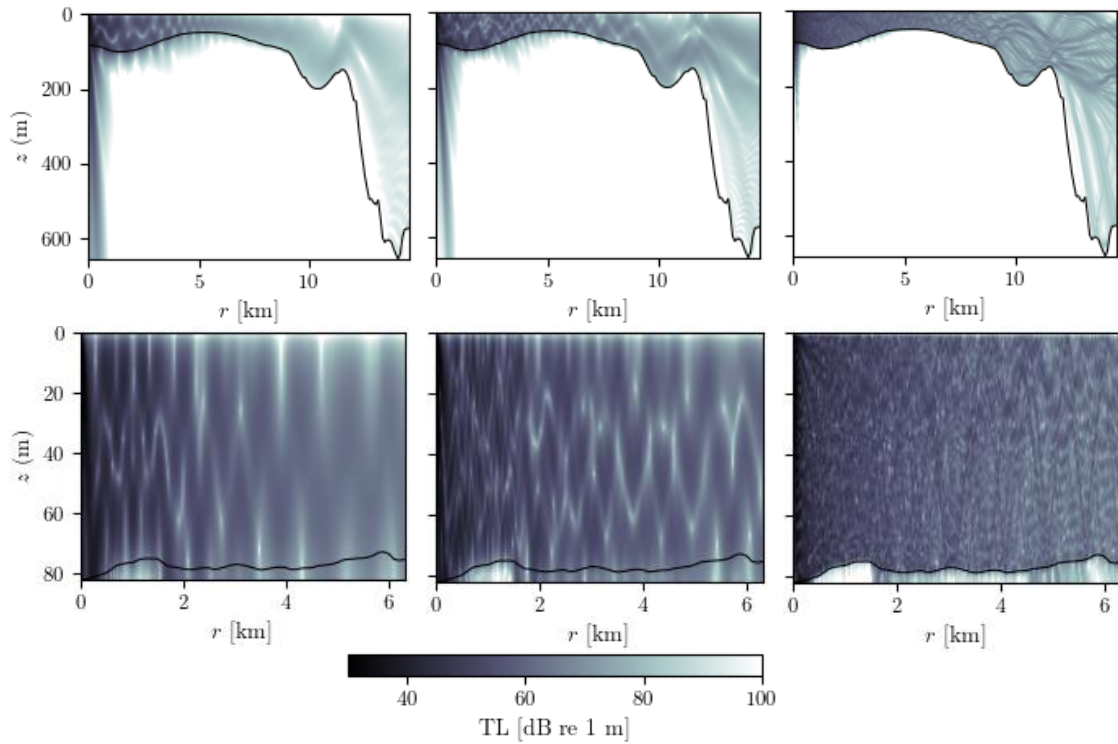
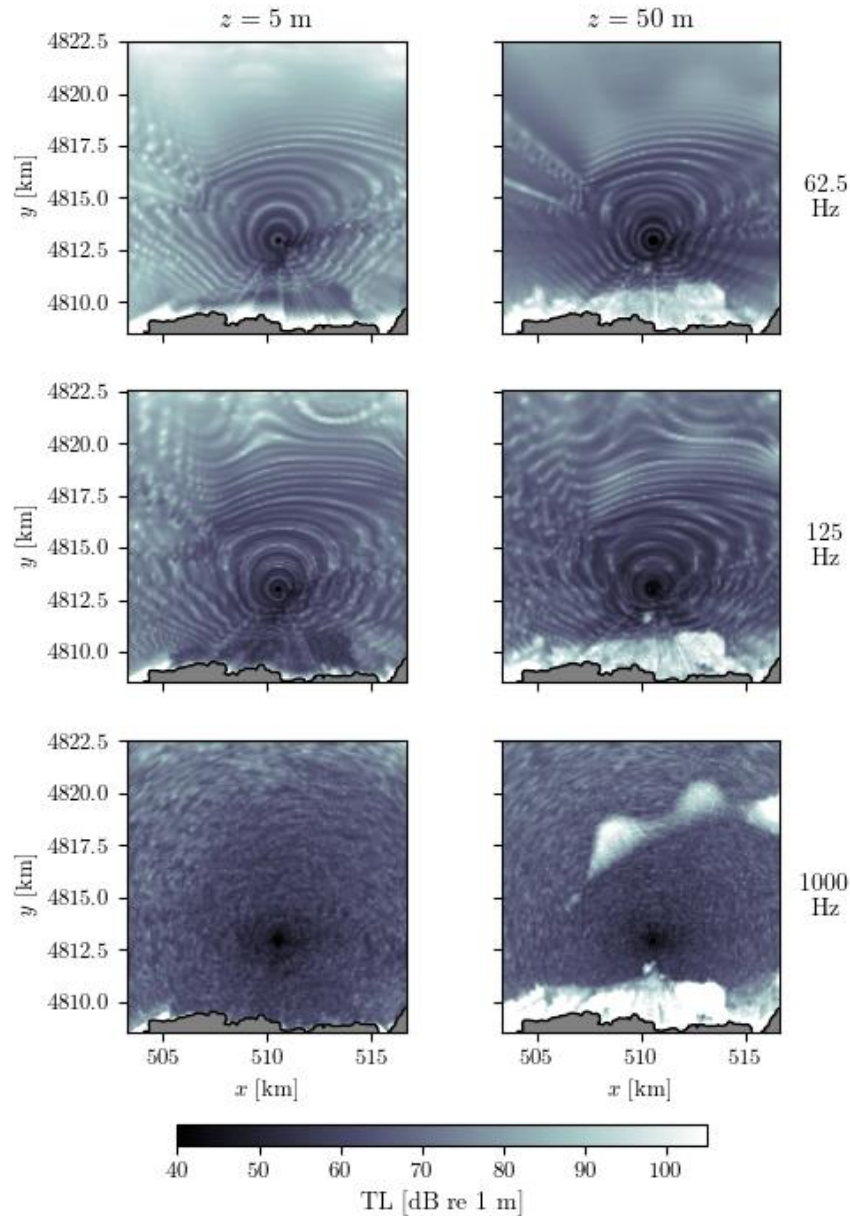


Figure 13. Samples of simulated TL along the transects of Figure 12. In the top row, the north-heading transect, while in the bottom row, the east-heading one. The columns denote the frequency: 62.5, 125 and 1000 Hz, from left to right.

In these first plots we can detect two characteristics of sound propagation in the sea: 1) as the frequency increases, the interference pattern becomes more homogeneous (e.g., the spacing between fringes becomes smaller); sound penetration into the seabed is also reduced, being the wave propagation more sensitive to bathymetry detail, and 2) as repeatedly discussed in previous sections, the propagation in shallow waters becomes inefficient for low frequencies.

Following the procedure given in the previous section, in Figure 14, TL fields for  $z = 5$  m and  $z = 50$  m are shown, for the three chosen frequencies of this study. The anisotropy of the field is noticeable, particularly for the lower frequencies. For these examples, the field is not masked yet (some cells show values inside seabed, compared with Figure 25, for instance).



**Figure 14.** Selected samples of Transmission Losses fields for the scenario of MARMOK-A-5.

In these plots it is clear that lower frequencies propagate poorer, reaching almost 100 dB re 1 m at 10 km distance (northern part); for the contrary, for 1000 Hz levels do not decay beyond around 80 dB re 1 m that same area.

In Figure 15 the average TL in depth is plotted for the selected frequencies. In this case, only values of TL in depths corresponding to water column are averaged. Although kind of faded now (the field becomes more diffuse), the averaging process does not erase all trace of interference patterns in these fields.

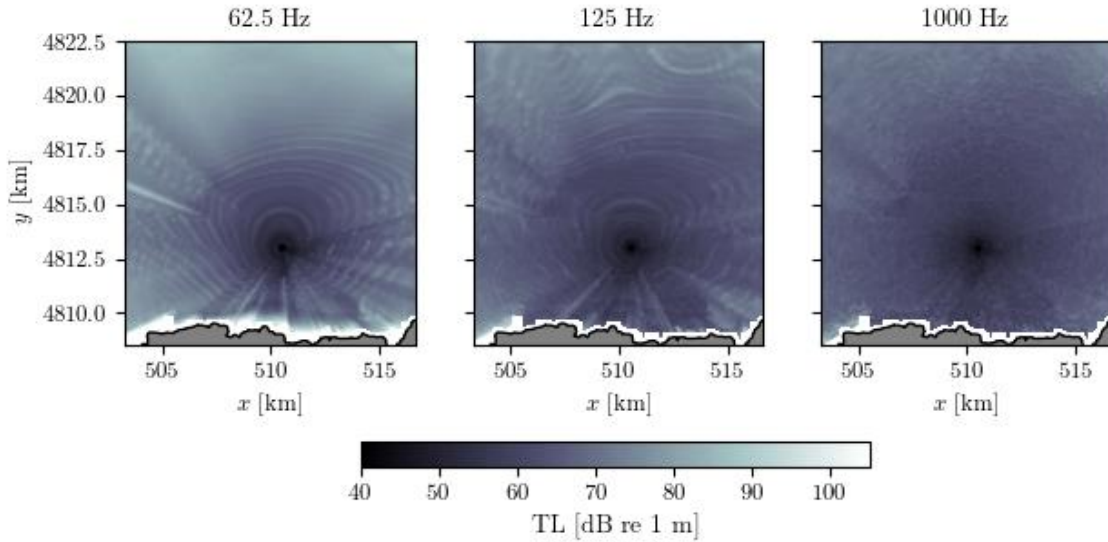


**Figure 15.** Selected samples of average (in depth) TL fields for the scenario of MARMOK-A-5.

#### 5.1.1.1 Fit to a geometric spreading loss model

In this complementary section, we will explore how well does the simple geometric spreading losses model describe the simulated data. In this regard, we fit lines by the least squares method of the type (it differs from a typical by in that no intercept is assumed)

$$y = a \log(r/r_1) \equiv ax \quad (5)$$

Thus,  $a$ , which is the coefficient that is usually equal to 20 (spherical spreading) or 10 (cylindrical spreading), is identified as the slope of the fitted line if plotted in logarithmic units (recall  $r_1$  denotes reference distance, which is equal to 1 meter).

In more detail, we have used the depth-averaged TL fields (for the three frequencies), from which the TL curves (on transects) are obtained. This kind of inverse interpolation (from the grid to transects) allows direct comparisons with the bathymetry. In this regard, to fit the curves correctly, every transect must be terminated if it encounters land or the seabed. Even then, in some cases the fit might not be adequate (e.g., for extremely shallow waters): this issue is thus more noticeable for the Mutriku scenario.

In Figure 16 examples of the fitted data are shown for a given transect.

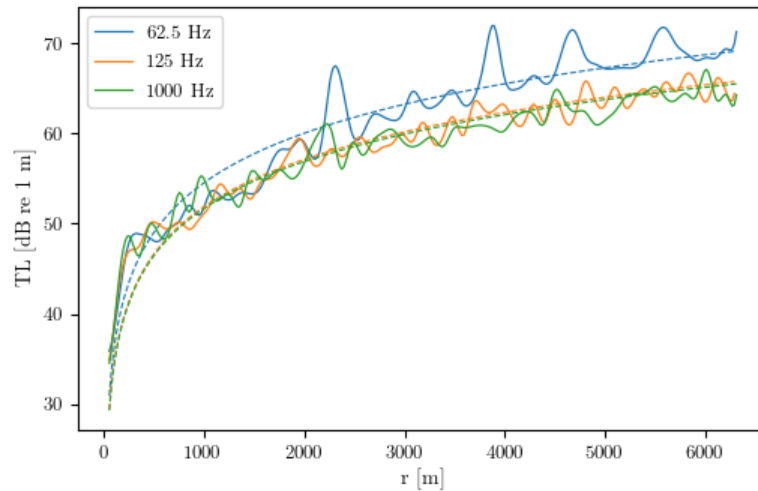


**Figure 16.** TL curves (solid: simulated data, dashed: fitted data) for the east-headed transect of **Figure 12**. The actual values of the coefficient (with  $R^2$ ) are: 18.597 (0.998), 17.309 (0.999), 17.201 (0.999), for the 62.5, 125, and 1000 Hz cases, respectively.

In the Figure 17, both the coefficient  $a$  and the R-squared parameter are shown for the three frequencies. From them and having in mind the bathymetry (Figure 5), we see that transects directed to deeper zones imply a greater value of  $a$ , close to 20 (as was expected – deep channels are characterized by a greater contribution of spherical propagation). Of course, the other extreme is also true, as those directions in which the propagation is poor (towards the coastline) imply an even greater coefficient. Towards the East and West, where the bathymetric profile is mostly constant, the coefficient takes a close value to 15 (that of cylindrical-spherical propagation). Furthermore, the coefficient for 62.5 Hz is higher than for 125 and 1000 Hz in all directions. Regarding the goodness of the fits (R-squared), we infer that transects towards the coastline give off smaller values (particularly for the 62.5 Hz case), a reflection of the poorer transmission of such low frequencies in shallow waters.

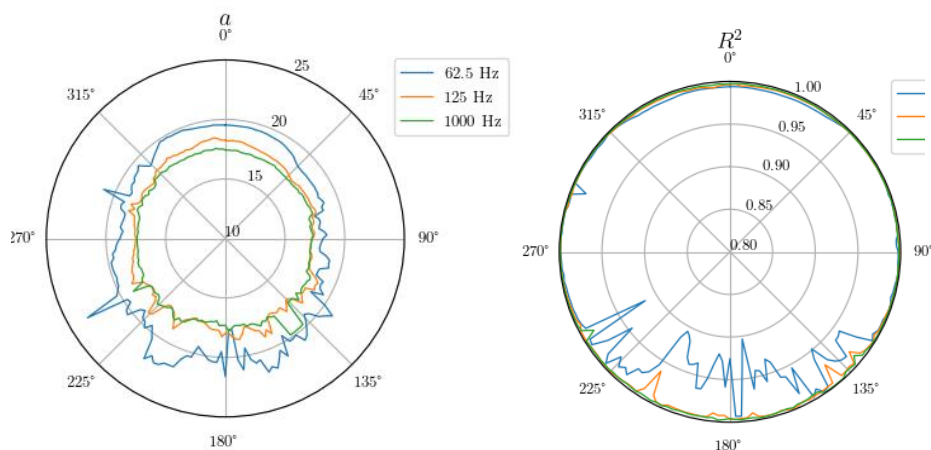


**Figure 17.** In the left (right), polar plot of the slope ( $R^2$  parameter) of the linear regression  $TL = ax$ , for MARMOK-A-5

In the Table 8 and Table 9 the mean values of the fit parameters in the four quadrants delimited by the cardinal directions are displayed. They reinforce the points discussed before.

**Table 8.** Main metrics of the slopes ( $a$  coefficient) of the fitted curves in the four quadrants delimited by the cardinal points, for MARMOK-A-5.

Direction	$f$ [Hz]					
	62.5		125		1000	
	Average	STD	Average	STD	Average	STD
N	19.43	0.28	18.07	0.22	17.43	0.13
E	18.69	0.69	17.64	0.38	17.41	0.22
S	20.50	0.99	17.83	0.49	17.75	0.75
W	19.42	0.80	17.75	0.34	17.54	0.25

**Table 9.** Main metrics of the  $R^2$  coefficient of the fitted curves in the four quadrants delimited by the cardinal points, for MARMOK-A-5.

Direction	$f$ [Hz]					
	62.5		125		1000	
	Average	STD	Average	STD	Average	STD
N	0.997	0.28	0.998	0.22	0.999	0.13
E	0.997	0.69	0.999	0.38	0.999	0.22
S	0.997	0.99	0.997	0.49	0.998	0.75
W	0.996	0.80	0.999	0.34	0.999	0.25

### 5.1.2 Mutriku

As done before, in the following figures two examples of transects of 15 km (Figure 18) have been selected and plotted in detail with their corresponding transmission losses fields in the vertical plane. It is notable how efficiently the shallow water channel filters out the lower frequencies, a particularity of the bathymetry, with a depth lesser than 20 m in the first kilometre.

Iterating through all transects (with an angular resolution of 2 degrees) and interpolating to a rectangular grid, we obtain a full description of the TL field in three dimensions (Figure 19). Operating as before, we select some depths to show the polar plots of the transmission losses, e.g.,  $TL(x, y)$ . As such, in Figure 20, TL fields for  $z = 5$  m and  $z = 50$  m are shown, for the three chosen frequencies of this study.

Because of the explicit shape of the SSP (decreasing with depth until 100 meters), it is coherent to find lower transmission losses at 50 m depth than for 5 m. Notice that some areas of the plots appear as completely white because of missing data, that is, when the depth of the slice is higher than maximum value of bathymetry for the whole transect in question.

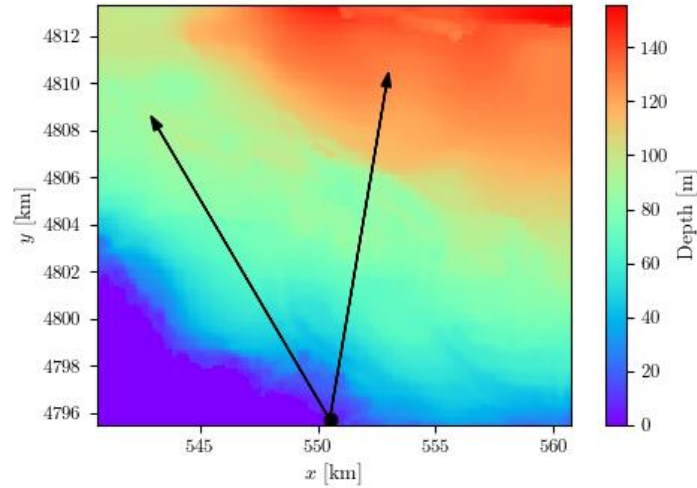


Figure 18. Samples of simulated TL along transects in the Mutriku scenario.

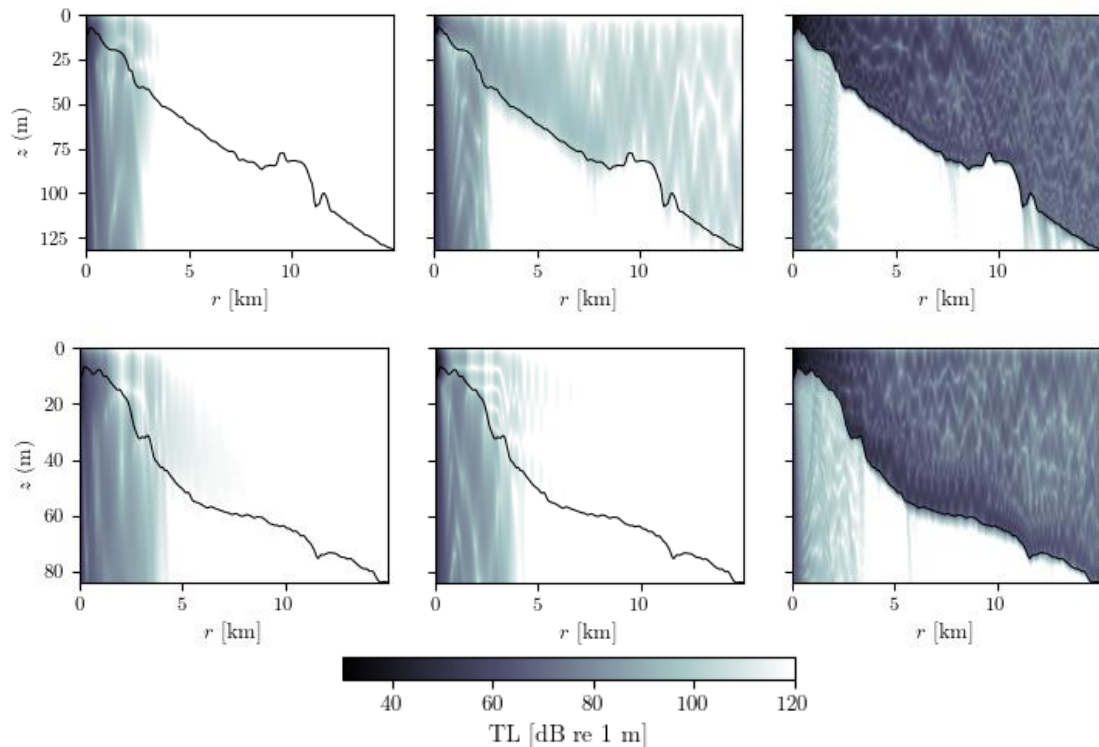


Figure 19. Samples of simulated TL along the transects of Figure 18. In the top row, the north-heading transect, while in the bottom row, the northwest-heading one. The columns denote the frequency: 62.5, 125 and 1000 Hz, from left to right.

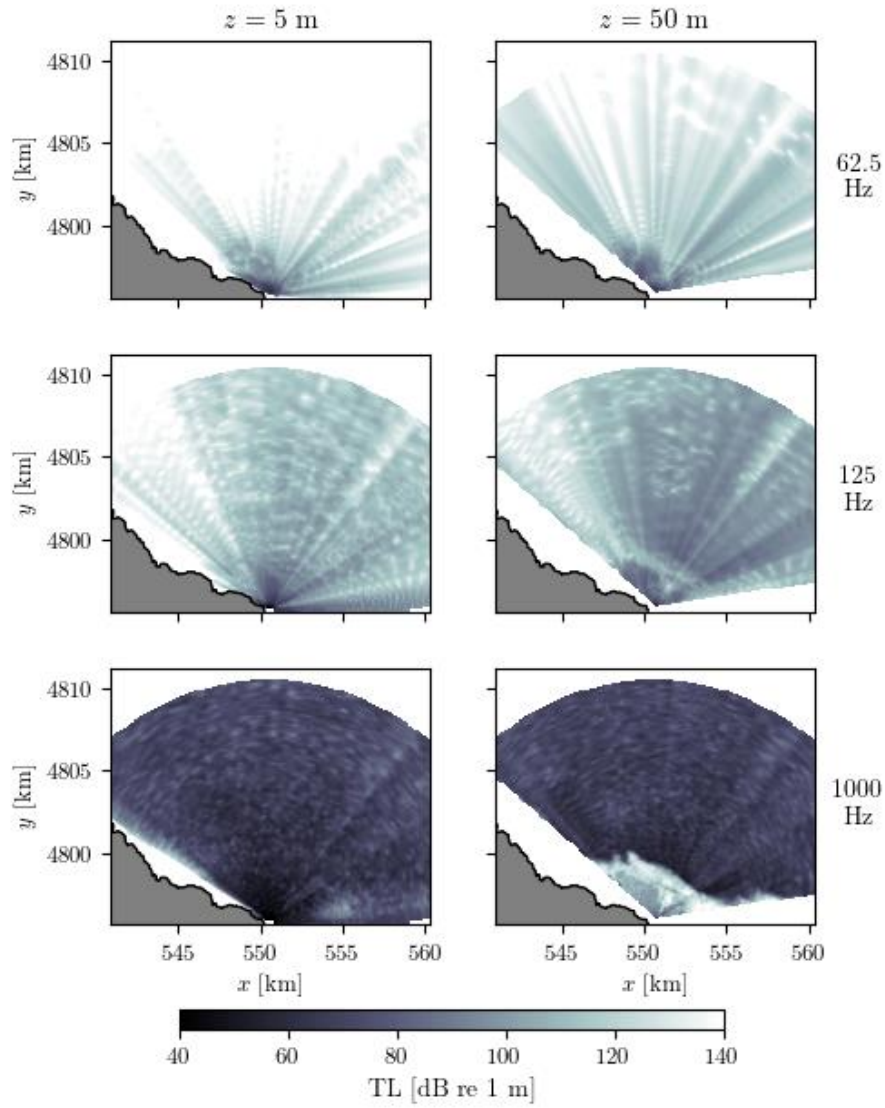


Figure 20. Transmission losses maps for Mutriku.

Correspondingly, the average transmission losses (in depth) fields are plotted in Figure 21.

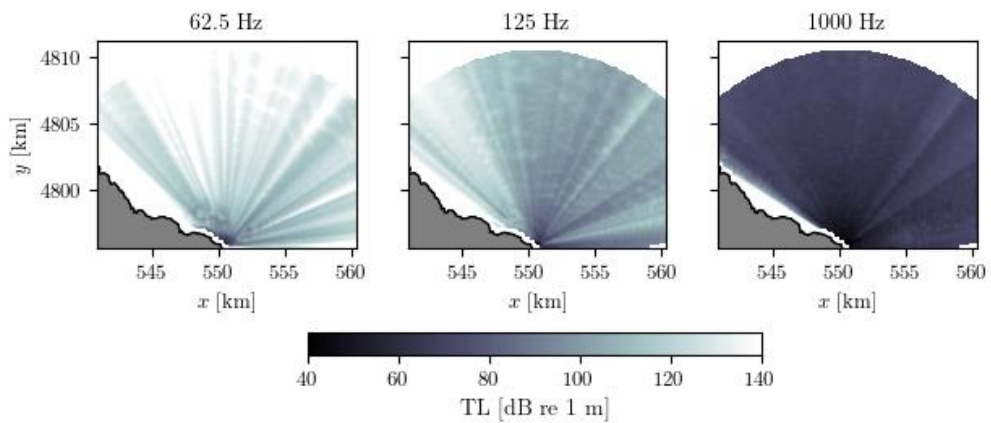
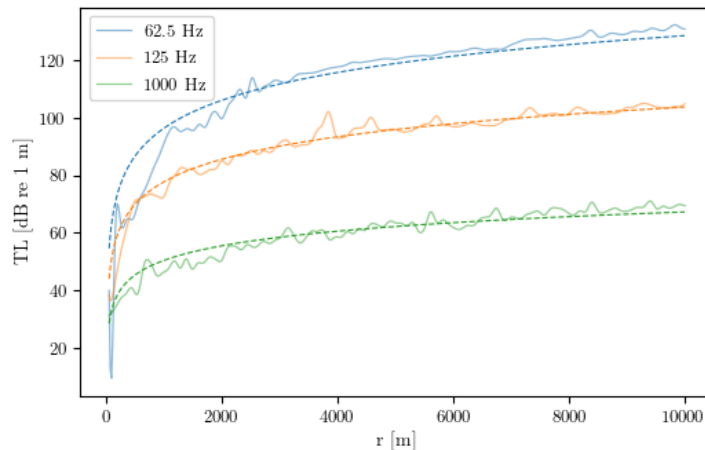


Figure 21. Average (in depth) transmission losses maps for Mutriku.

### 5.1.2.1 Fit to geometric spreading losses model

As done for MARMOK-A-5 in section 5.1.1.1, we explore here how well the radial dependence (from the source) these transmission losses can be modelled by a geometric spreading losses model (given by equation (3)). Following the same procedure as in that case, in Figure 22 the depth-averaged TL curves corresponding to the northeast-headed transect of Figure 18 are shown with their respective fitted curves.



**Figure 22.** TL curves (solid: simulated data, dashed: fitted data) for the northeast-headed transect of Figure 18. The actual values of the coefficient (and  $R^2$ ) are: 32.139 (0.997), 25.931 (0.999) and 16.824 (0.998), for the 62.5, 125, and 1000 Hz cases, respectively.

Polar plots of the fitted parameters are shown in Figure 23, in which the spanned angles are restricted by the land. Remarkably, on the one hand, the coefficient  $a$  is very high in general ( $> 20$ , i.e., hyper-geometric propagation) except for the case of 1000 Hz (in which it is between 15 and 20), reflecting the low-frequencies filter phenomenon characteristic of shallow waters (recall that the source is practically on-shore in this scenario); on the other hand, the  $R^2$  parameter is relatively good except for the transects closer to the coastline, for which  $a$  dramatically increases as well.

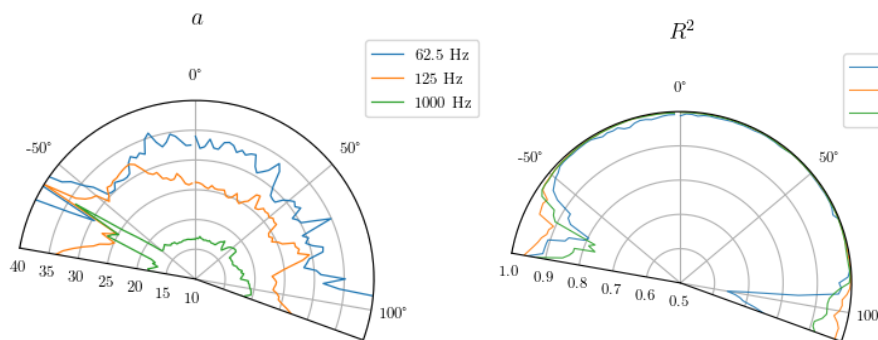


**Figure 23** Polar plots of the slope (left) and the  $R^2$  parameter (right) of the linear regression  $TL = ax$ , for Mutriku.

Finally, in the following tables, as not all the cardinal points are among the spanned transects, we have selected two specific directions: those with steepest and more constant bathymetric profiles. With an angular width of 4 degrees around each chosen transect by these criteria ( $34^\circ$  and  $300^\circ$  - equivalently,  $-60^\circ$ , degrees respectively), the averaged parameters of the fits of the included transects are calculated. Since in this specific case, the constant bathymetric profile is more or less parallel to the coastline, and thus its mean depth is extremely low, the  $\alpha$  coefficient in this case is greater than the for the other (the steepest bathymetric profile is roughly found in the perpendicular direction from the coastline).

**Table 10.** Main metrics of the slopes ( $\alpha$  coefficient) of the fitted curves for the directions with steepest and more constant bathymetric profiles, for the Mutriku scenario.

Direction	$f$ [Hz]					
	62.5		125		1000	
	Average	STD	Average	STD	Average	STD
Steepest bathymetry	31.96	1.27	25.80	1.04	17.25	0.41
Constant bathymetry	38.95	8.02	29.73	5.96	27.73	3.52

**Table 11.** Main metrics of the R-square coefficient ( $R^2$ ) of the fitted curves for the directions with steepest and more constant bathymetric profile, for the Mutriku scenario.

Direction	$f$ [Hz]					
	62.5		125		1000	
	Average	STD	Average	STD	Average	STD
Steepest bathymetry	0.998	0.001	0.999	0.000	0.999	0.0
Constant bathymetry	0.924	0.018	0.980	0.001	0.965	0.014

## 5.2 Source levels

As was anticipated in section 4.4, here we show the results from the backpropagation carried out to find out source levels in dB and make possible the calculation of sound pressure level maps. The details for each scenario are presented in the following subsections.

It is worth mentioning that these source level values can be taken as upper bound to the actual values, as no background noise contribution is considered when backpropagating the measured values.

### 5.2.1 MARMOK-A-5

In the case of MARMOK-A-5, we should recall that the distance between the fixed hydrophone (temporal monitoring) and converter was approximately only 90 meters. Because of this very close distance, a spherical divergence model was applied for this case, resulting in the values shown in Table 12.

**Table 12.** TL at the location of the fixed hydrophone at BiMEP (MARMOK-A-5 case) [dB re 1 m].

TL [dB re 1 m]	<i>f</i> [Hz]		
	62.5	125	1000
	31.8	32.0	32.8

Using these values, the source level values for the three frequencies can be calculated using equation (4), and are shown in Table 13).

**Table 13.** SL values of the MARMOK-A-5 converter [dB re 1  $\mu$ Pa].

<i>H<sub>w</sub></i>	<i>f</i> [Hz]		
	62.5	125	1000
[0,1)	140.7	132.6	127.8
[1,2)	143.6	134.6	130.7
[2,5)	144.8	137.7	136.3

### 5.2.2 Mutriku

For the case of Mutriku, since the distance from the source is 1 km, far field conditions are met, and we can use the already calculated TL fields to find the corresponding value at the hydrophone location. These values are presented in Table 14.

**Table 14.** TL values at the location of the fixed hydrophone in Mutriku [dB re 1 m].

TL [dB re 1 m]	<i>f</i> [Hz]		
	62.5	125	1000
	86.8	76.2	56.2

The equivalent Source Level for Mutriku is shown in the Table 15.

**Table 15.** SL values of the Mutriku power plant [dB re 1  $\mu$ Pa].

<i>H<sub>w</sub></i>	<i>f</i> [Hz]		
	62.5	127	1000
[0,1)	164.2	155.3	169.3
[1,2)	166.1	157.0	139.1

[2,5)	169.3	160.1	141.4
-------	-------	-------	-------

However, it is particularly necessary in this case (since there was no significant sound emission from the device, as deduced in the analysis of deliverable 2.3) to reiterate that these calculations assume that the measured values from which are obtained  $SPL_{on}$  are only due to the device noise, when in reality there is always the contribution of background noise.

### 5.3 Sound pressure levels

As explained in section 4.4, the sound pressure levels are obtained by simply subtracting the TL fields obtained in section 5.1 from the just presented SL values. As three different wave height classifications were made (SL depends on this variable), there will be three SPL fields for every frequency and depth of simulation.

We will also find the level curves characterized by the equality  $SPL = SPL_{off}$ , which will define the acoustic influence zones of each converter and shall be further explained in the “Metrics” sections; these will be denoted as iso-acoustic curves.

#### 5.3.1 MARMOK-A-5

From the analysis of acoustic measurements carried out in D2.3 it was deduced that the operation of MARMOK-A-5 added some noise to the background soundscape, so it is expected to obtain some levels over background levels, at least in the immediate neighbourhood of the device.

##### 5.3.1.1 Sound maps

First, we repeat the same type of maps as in section 5.1, but for SPL, to obtain absolute noise values, in a contour fashion, showing the acoustic disturbance area of each scenario: (i)  $H_w < 1$  scenario (Figure 25); (ii)  $1 \leq H_w < 2$  scenario (Figure 26) and (iii)  $H_w \geq 2$  scenario (Figure 27). A detailed example is illustrated in Figure 24.

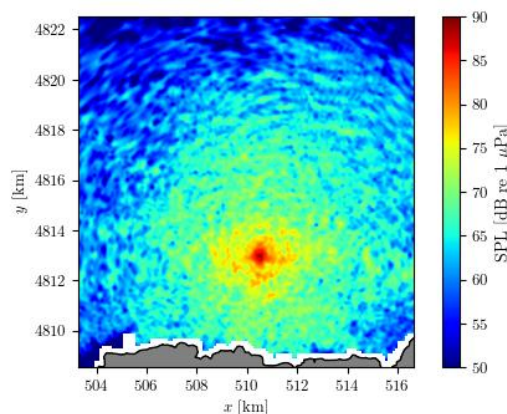


**Figure 24.** Detail of SPL sound map. In this example, mean (in depth) SPL for 1 kHz,  $z = 5$  m, for a SL of 127.8 dB re 1  $\mu$ Pa (corresponding to the case with  $H_w < 1$ ).

$$H_w < 1$$

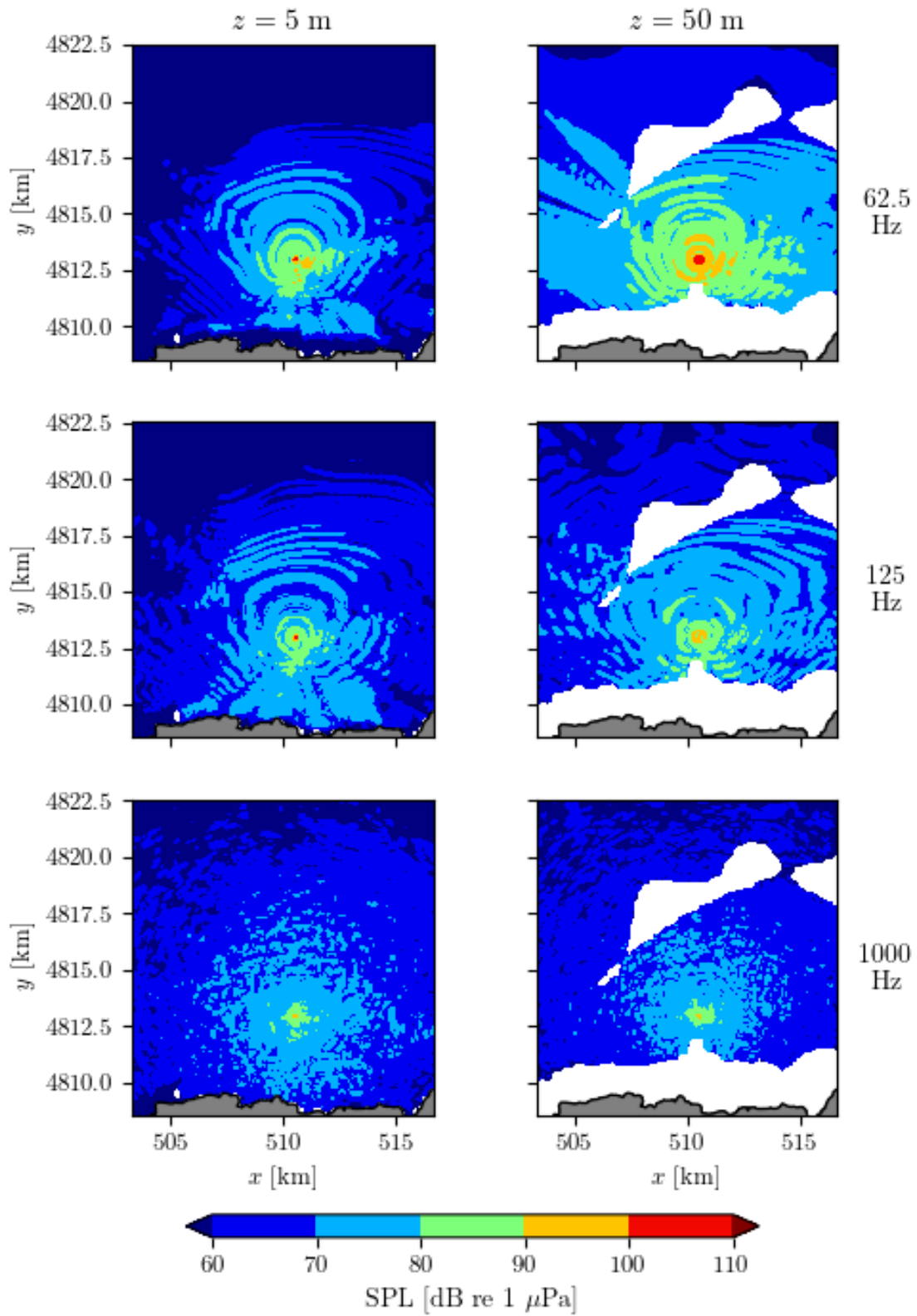


Figure 25. Sound pressure level sample polar plots for MARMOK-A-5 in the  $H_w < 1$  scenario.

$$1 \leq H_w < 2$$

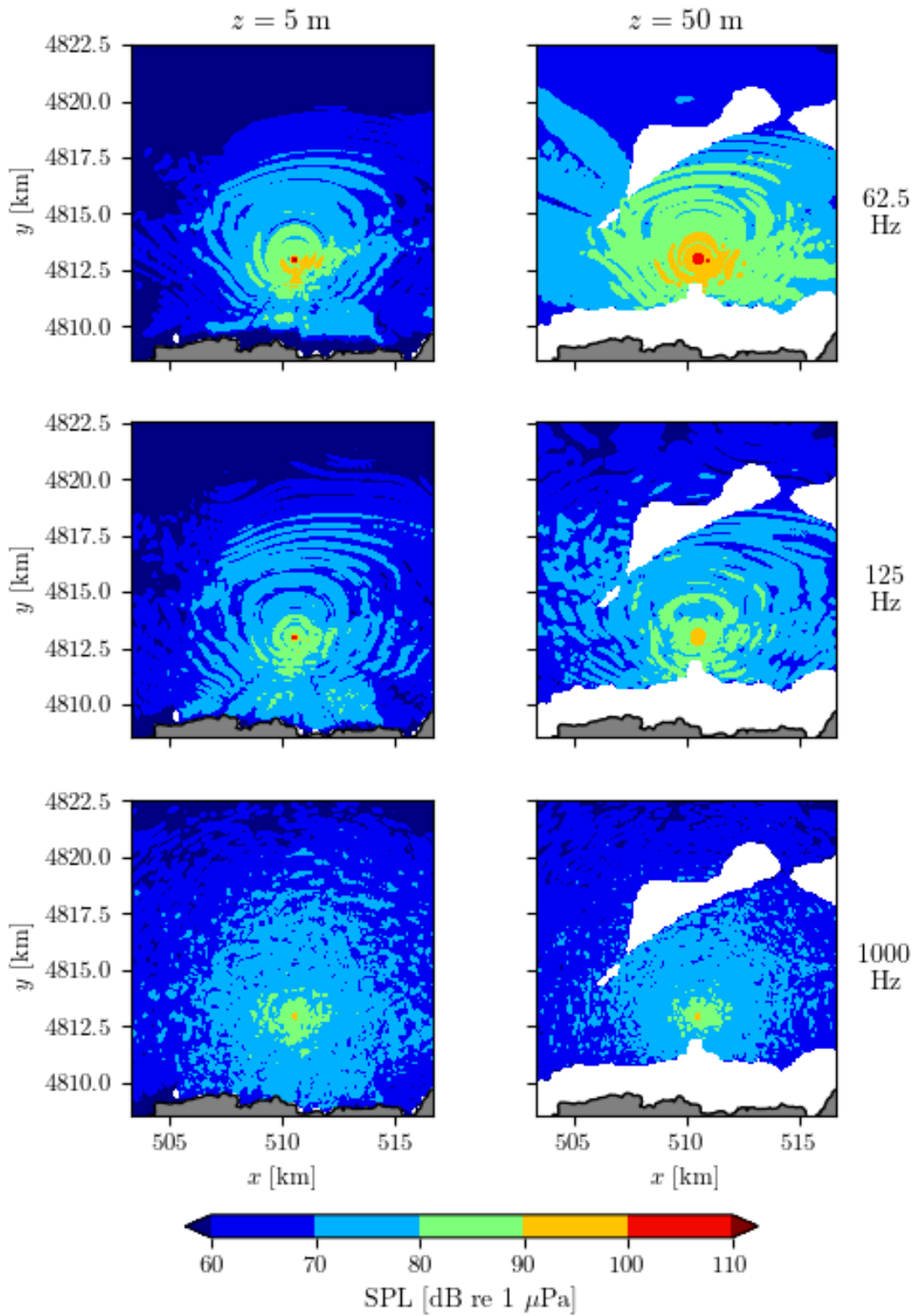


Figure 26. Sound pressure level sample polar plots for MARMOK-A-5 in the  $1 \leq H_w < 2$  scenario.

$$H_w \geq 2$$

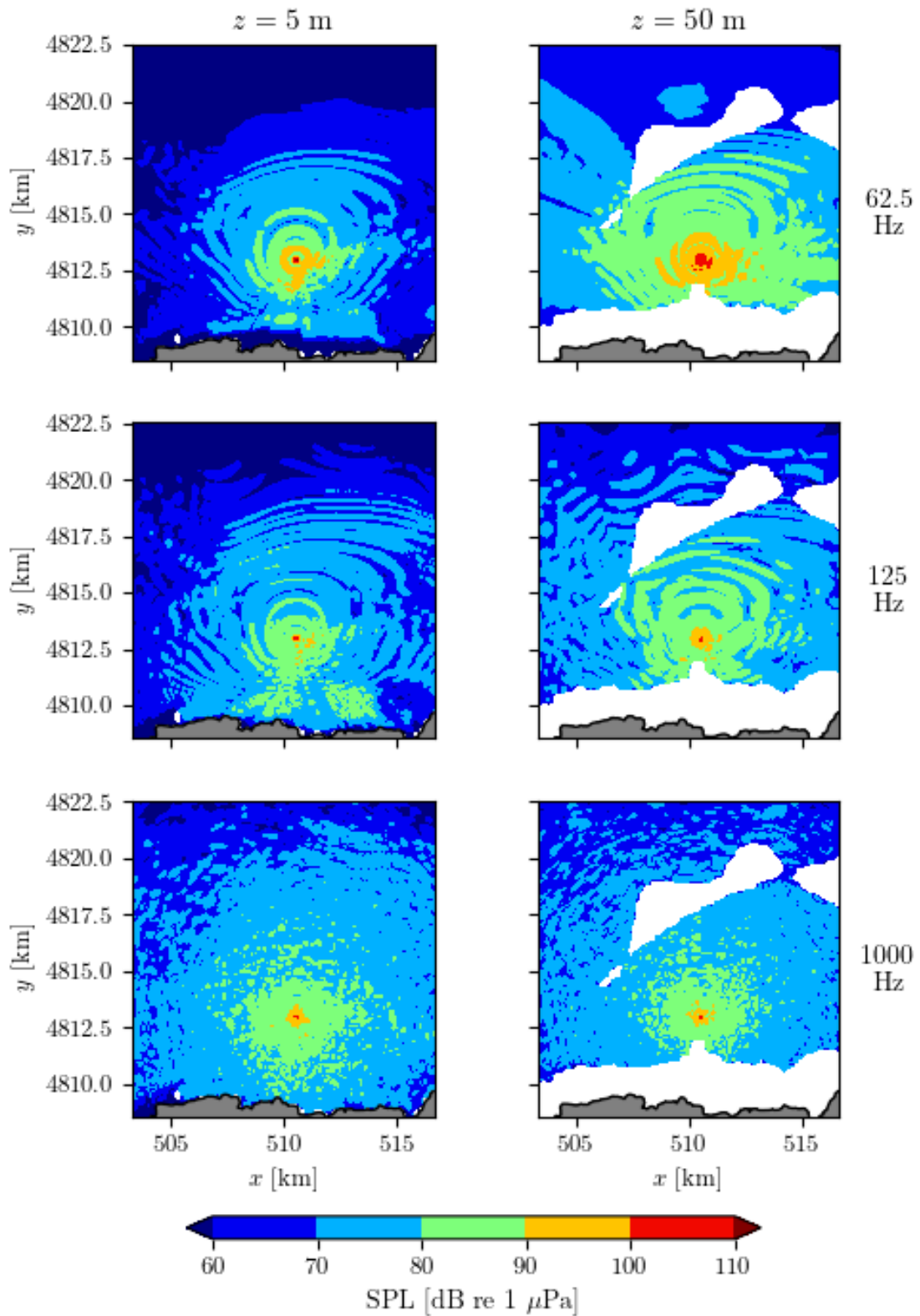


Figure 27. Sound pressure level sample polar plots for MARMOK-A-5 in the  $H_w \geq 2$  scenario.

As can be easily seen in this contour plots, the SPL distribution quickly reaches low levels for all cases, but even more for the lower frequencies (although the near-field values are higher in this case, due to the higher source level) and wave heights; regarding the dependence in depth, and in agreement with the results from section 5.1.1, the values increase for the 50 m depth plane.

Analogously, the averaged (in depth) SPL field (henceforth denoted as case 1) is shown in

Figure 28, which also features more zoom. These plots also show (as a black contour line) the isoacoustic defined by the background noise level, for direct comparison between the two regimes. However, because of the relatively low emission sound levels, these lines encompass areas very small around the converter.

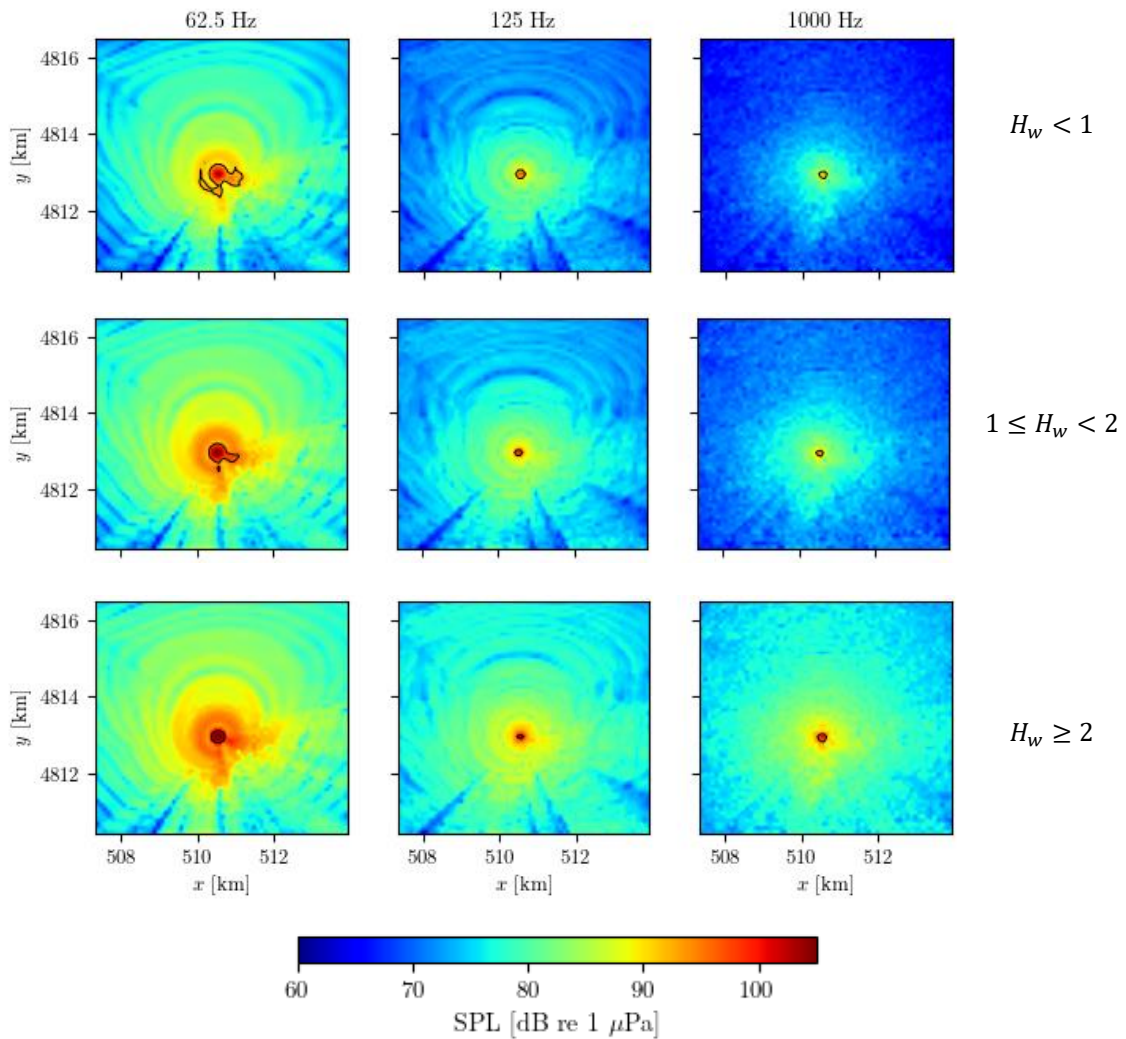


Figure 28. Average (in depth) Sound Pressure Level for the MARMOK-A-5 case.

The averaged in depth SPL increases as wave height and the acoustic wavelength do, with the higher levels found at  $H_w \geq 2$  and 62.5 Hz.

Moreover, in the

Figure 29 (again with more zoom in the position of the converter), we select the  $z$  planes in which the spatially (horizontal plane) averaged SPL are greater, for each frequency (henceforth denoted as case 2).

These are 40, 50, 50 meters, for 62.5, 125 and 1000 Hz, respectively. Again, the isoacoustic defined by the background noise level is plotted as a black contour line for direct comparison between the two regimes.

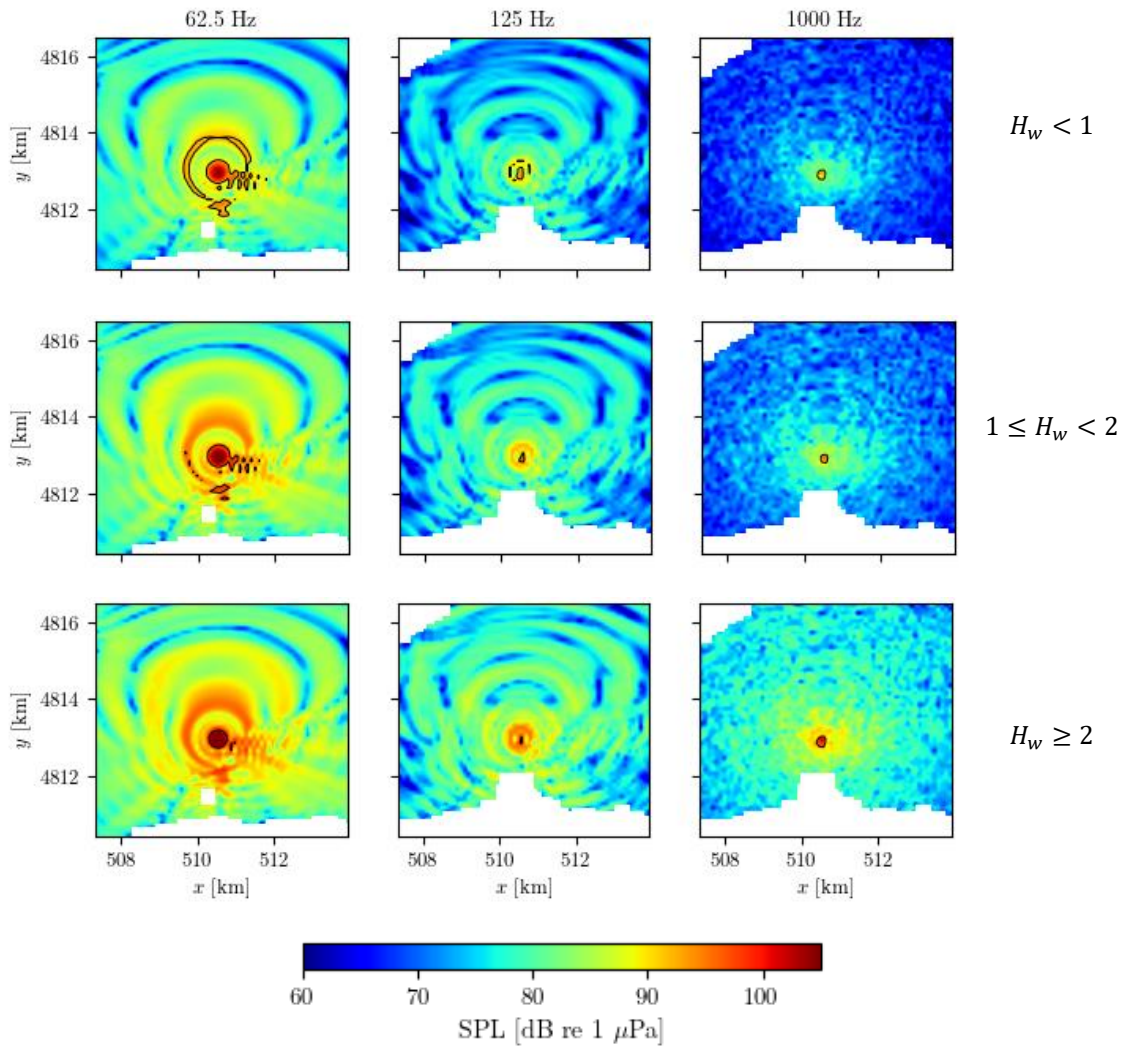


Figure 29. SPL maps for the depths with highest average SPL value in the case of MARMOK-A-5 (40, 50, and 50 m from left to right).

### 5.3.1.2 Metrics

We proceed now to obtain some useful metrics for the characterization of the **SPL** fields around the device. First, we calculate the area encompassed by the iso-acoustic curves (points where  $SPL_{on}$  is equal to  $SPL_{off}$ ) in every scenario; this describes the susceptible area in which the **SPL** is greater than the natural background noise (denoted as  $S$ ). In particular, we do this for the depth-averaged **SPL** and for the depths of maximum spatially averaged **SPL**, as corresponding to

Figure 28 and

Figure 29. The results are shown in Figure 30.

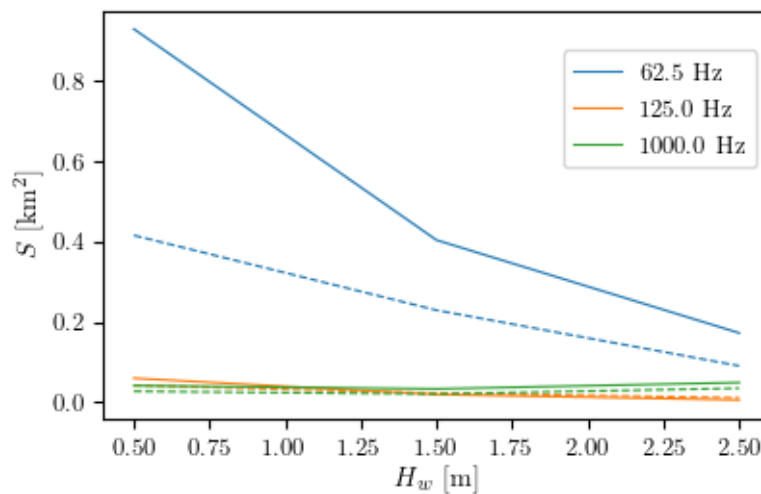


**Figure 30.** Surface area of disturbance for the MARMOK-A-5 scenario, for the case 1 (dashed line) and case 2 (solid).

Another metric of interest is the dependence of **SPL** with radial distance. This can be obtained by calculating the average **SPL** in concentric annuli around the sources. The results of such procedure are shown in Figure 31, the average value in depth of these values (for every frequency and wave height bin) has been computed, as well as the baseline background noise levels (as dashed lines). Note how there is only one frequency for which the so calculated mean sound pressure levels are greater (up to around 200 m from the converter) than the respective baseline values: 62.5 Hz.

The exact distances at which these levels are equal are displayed in Table 16 for this case. These are simply obtained by finding the intersection between the dashed and solid lines in the previous plots.

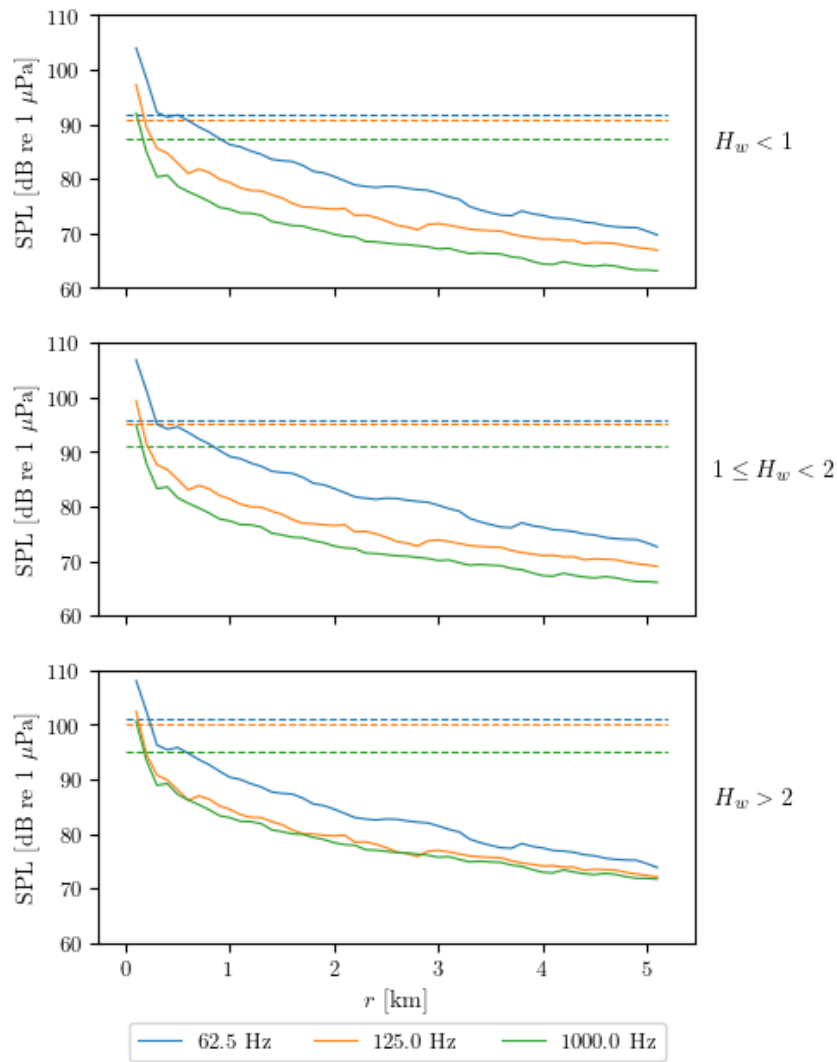


**Figure 31.** Average value in depth of SPL (case 1) sampled in concentric annuli around the MARMOK-A-5 device (solid) with corresponding  $SPL_{off}$  (dashed).

**Table 16.** Distances (m) from the device at which the mean of the depth-averaged SPL field drops below  $SPL_{off}$ .

$H_w$	$f$ [Hz]		
	62.5	125	1000
[0,1)	240.6	103.2	82.1
[1,2)	216.1	81.7	73.8
[2,5)	152.3	64.7	89.2

Analogously, the same metric is calculated for the case 2, which results can be seen in Figure 32.

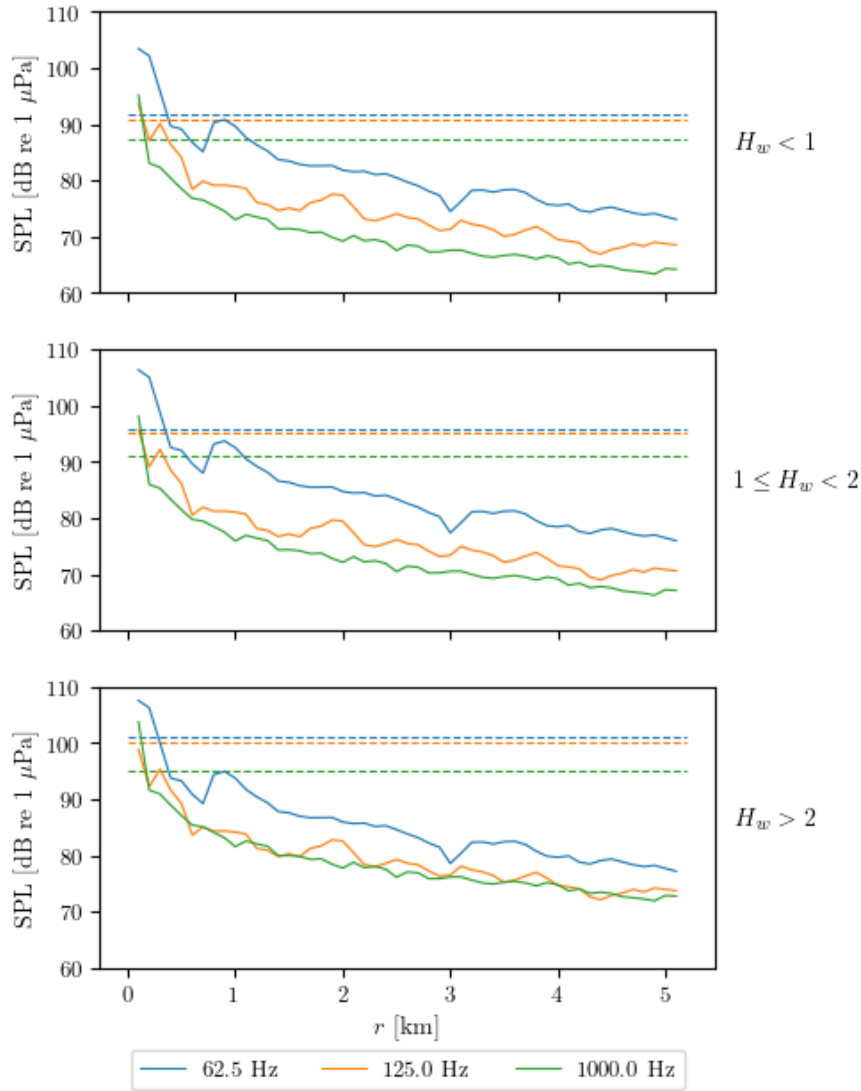


**Figure 32.** Average value of SPL (for the case 2) sampled in concentric annuli around the MARMOK-A-5 device (solid) with corresponding  $SPL_{off}$  (dashed).

Finally, the exact distances at which the sound levels are equal to the background noise levels for this case are shown in Table 17.

**Table 17.** Distances (m) from the device at which the mean of the selected depths SPL fields drop below  $SPL_{off}$  (case 2) for MARMOK-A-5.

$H_w$	$f$ [Hz]		
	62.5	125	1000
[0,1)	279.6	57.6	85.8
[1,2)	267.1	30.5	82.1
[2,5)	211.5	13.7	89.2

### 5.3.1.3 Multiple sources

Additionally, now we address the effect of adding several devices to the area as an array. In particular, 80 prototypes of converters are considered, clustered in 4 groups of 20 converters each. To find the SPL fields we use here the source level values in Table 13 and an analytical model of acoustic propagation, the geometric losses model, given by

$$TL(r) = a \log_{10}(r) + \alpha r$$

where  $\alpha$  is the absorption coefficient and  $a$  is obtained from the analysis of section 5.1.1.1 as the average of the values obtained therein: 19.51, 17.85 and 17.53 for 62.5, 125 and 1000 Hz, respectively. Depending on whether total coherence or incoherence is considered, the SPL fields differ (in a constant value) in about 20 dB re 1  $\mu$ Pa; here we focus on the incoherent case. Also, the considered depth shown in the maps is 20 meters. The results are shown in Figure 33.

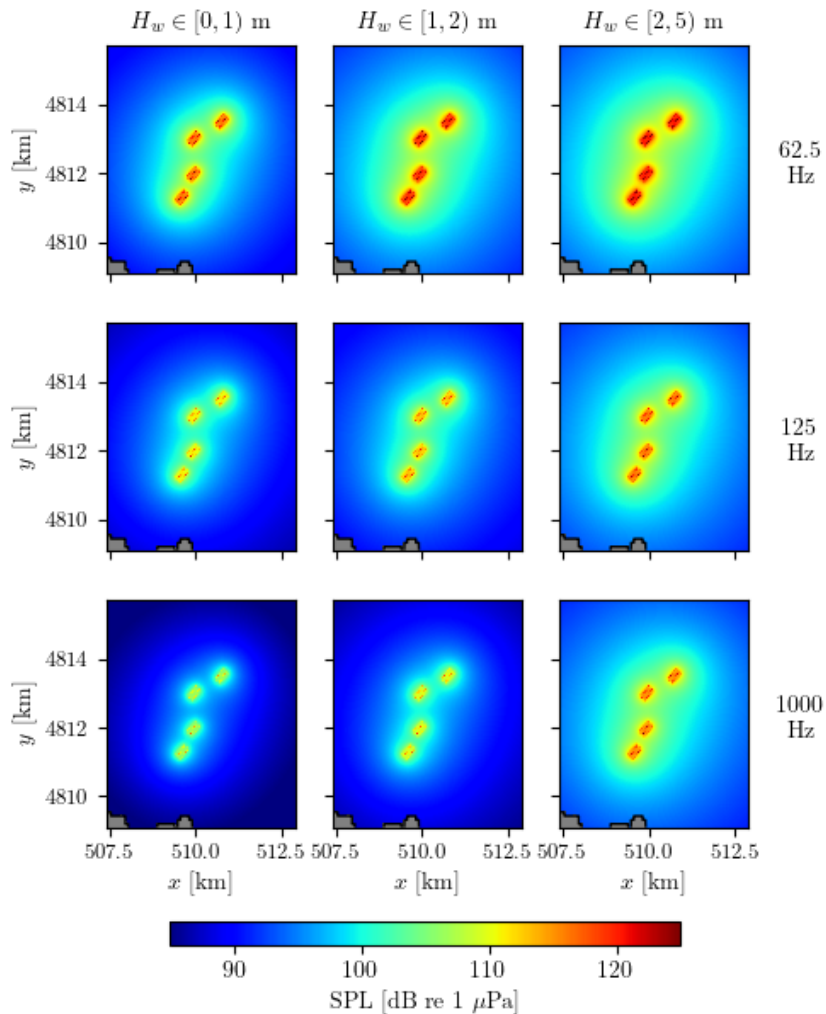


**Figure 33.** Sound maps for the hypothetical MARMOK-A-5 swarm, for a depth of 20 meters (incoherent case).

As expected, higher values are found for low frequencies and high wave heights, as this model does not take into account the bathymetry (and thus, there is no low-frequency filtering effect).

In Figure 34 we compare this scenario against one with just one WEC in the middle of the ensemble with the same values of SL as the individual WECs of the swarm. The higher differences in SPL are found, again, for the low frequencies and higher wave heights, with maximum values up to 50 dB re 1  $\mu\text{Pa}$ .

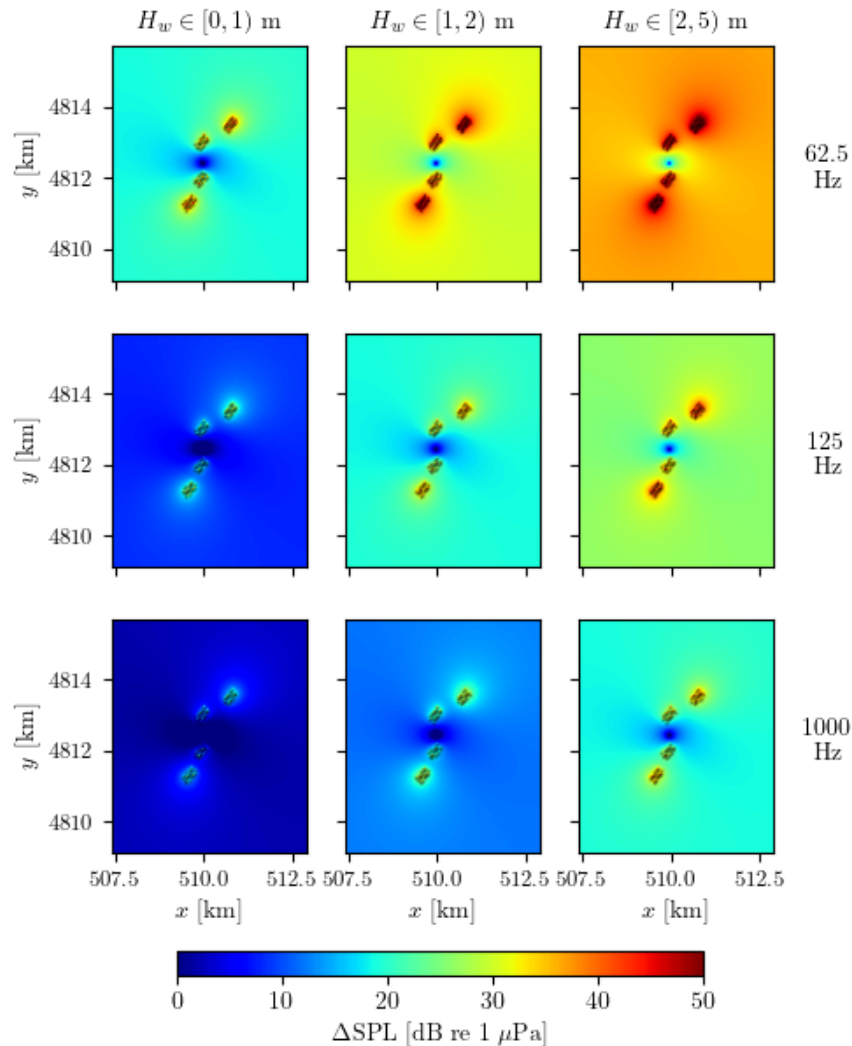


**Figure 34.** Difference in SPL between the hypothetical MARMOK-A-5 swarm and the same device in the centre of the region (incoherent case).

We now show (Figure 35) the radial distance (from the centre of the region) at which the sound pressure level fields are indistinguishable from the background noise levels, in the same way as done in the section before; the distances are now much greater though, with maximum values for low wave heights (where there is less background noise) and frequencies around 3.4 km.

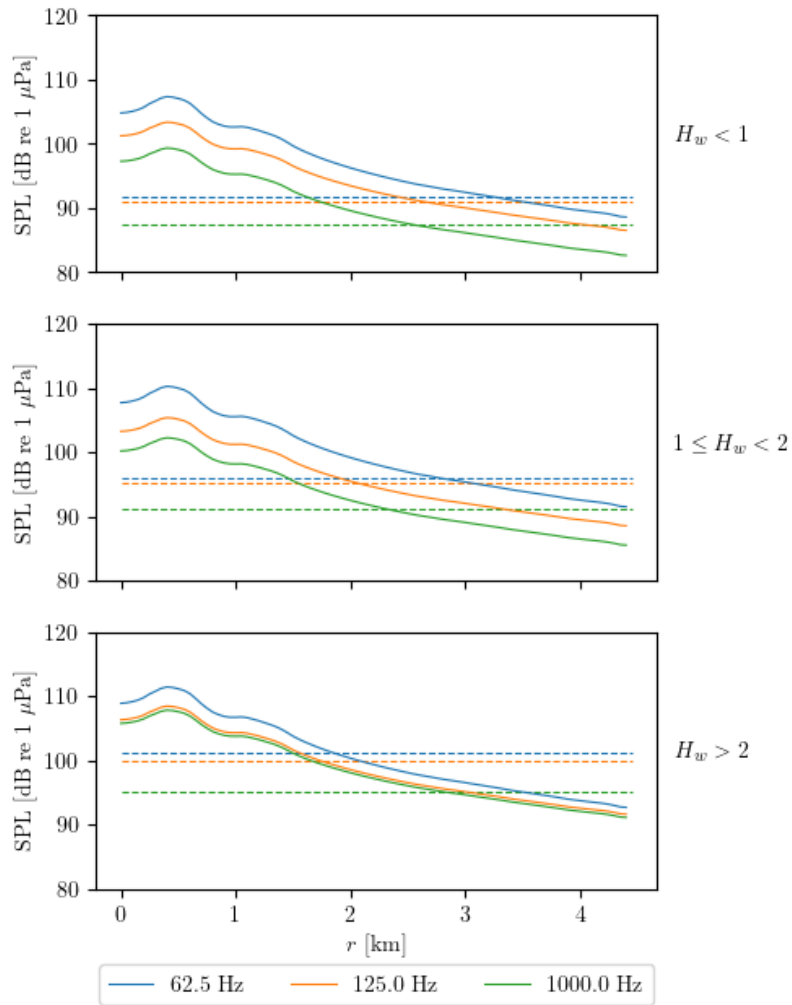


Figure 35. Average (in annular regions) SPL for the swarm (solid) and background noise levels (dashed).

In addition, in Figure 36, the area of disturbance (calculated as the area of the circle with radius given by the values of  $r$  at which  $SPL_{off}$  and  $SPL_{on}$ ) is plotted against the wave height for the three frequencies considered in this study, reinforcing the points previously discussed.

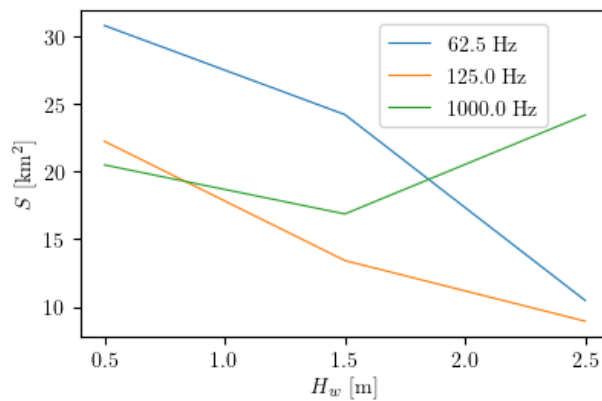


Figure 36. Surface area in which SPL values are greater than the corresponding  $SPL_{off}$ .

### 5.3.2 Mutriku

For the Mutriku power plant we did not find any clear evidence of noise at 1 km of distance, as deduced in D2.3. This was mostly expected, since shallow waters filter out low frequencies (in which most of the acoustic energy radiated by the structure is presumably centred), as mentioned previously.

#### 5.3.2.1 Sound maps

In this section, the SPL maps for the Mutriku case are presented. As source level values depend on wave height, and three bins have been considered, there will be three maps for every frequency and depth showing the acoustic disturbance area of each scenario: (i)  $H_w < 1$  scenario (Figure 38); (ii)  $1 \leq H_w < 2$  scenario (Figure 39) and (iii)  $H_w \geq 2$  scenario (Figure 40). In any case, recall that since the sound pressure level is simply obtained by subtracting the TL fields to the corresponding SL, the difference between maps of varying wave height will be a constant offset given by the difference in SL associated to such wave heights. A detailed example is illustrated in Figure 37.

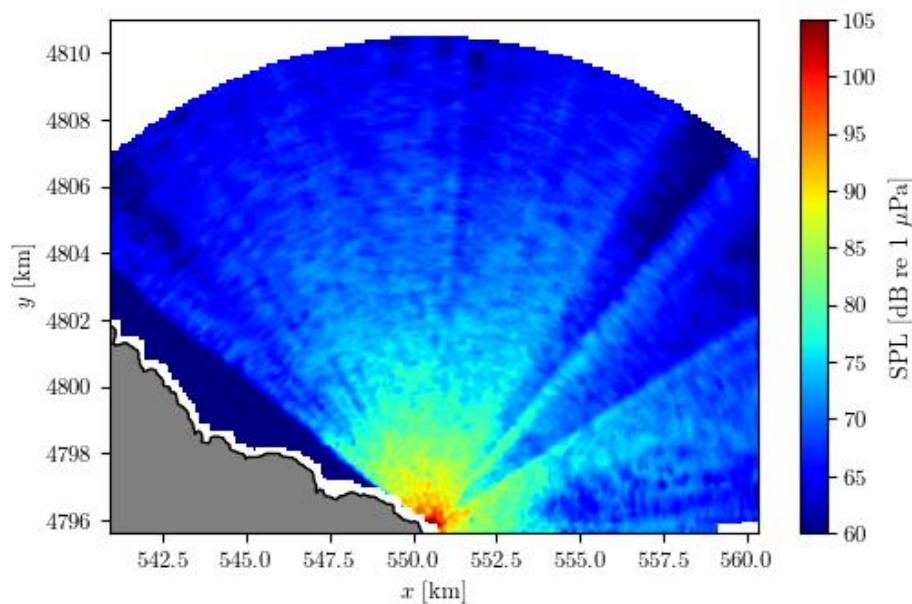


**Figure 37.** Detail of SPL polar plot. In this example, mean (in depth) SPL for 1 kHz,  $z = 5$  m, for a SL of 137.6 dB re 1  $\mu$ Pa (corresponding to the case with  $H_w < 1$ ).

In the following graphs, and as performed in the case of the MARMOK-A-5 device, we do not take into account those cells of the grid with an associated bathymetry above the sampling depth; these cells can be easily detected for the case with 50 meters depth, as a white stripe surrounding the coastline.

$$H_w < 1$$

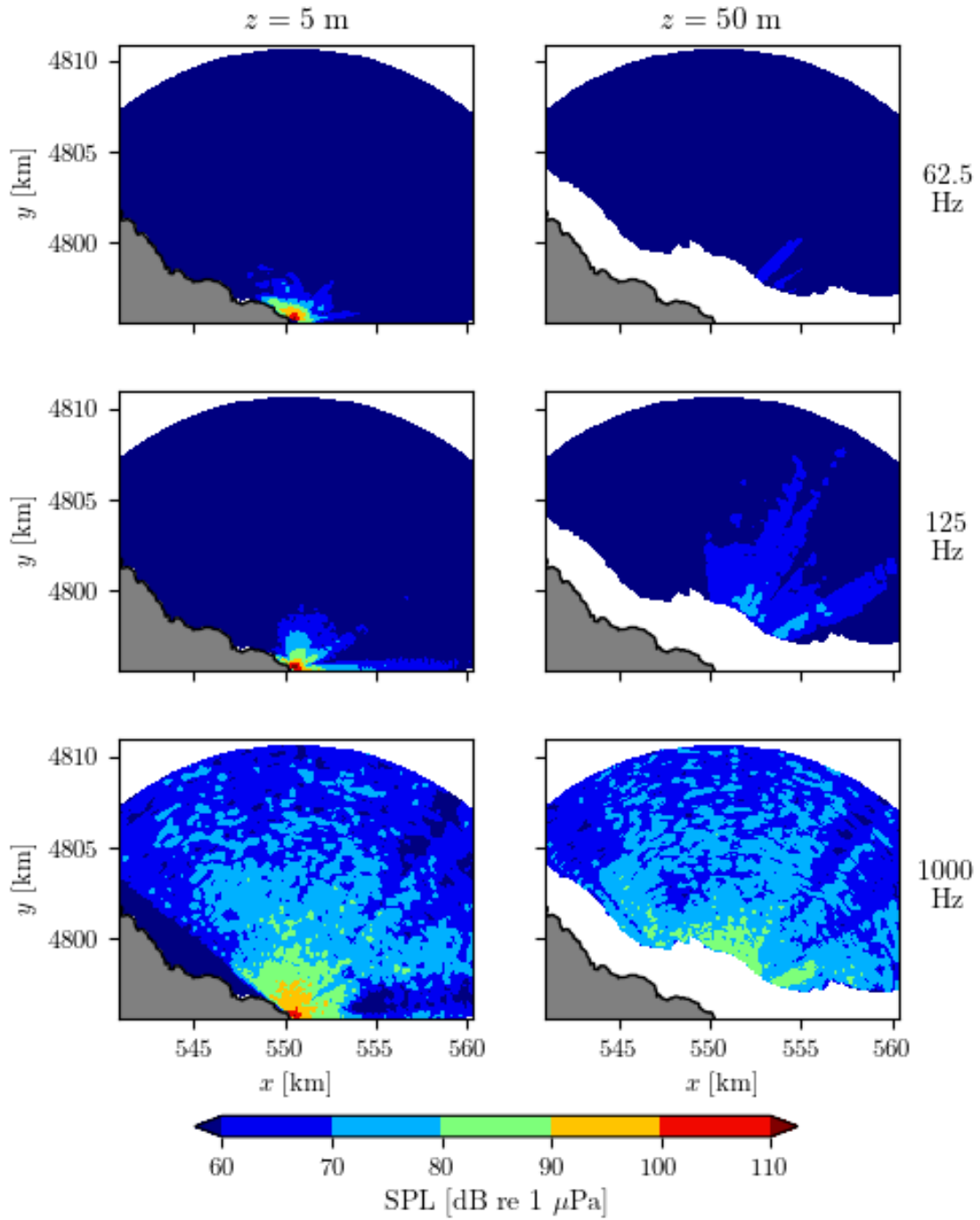


Figure 38. SPL maps for  $H_w < 1$  m in the Mutriku scenario.

$$1 \leq H_w < 2$$

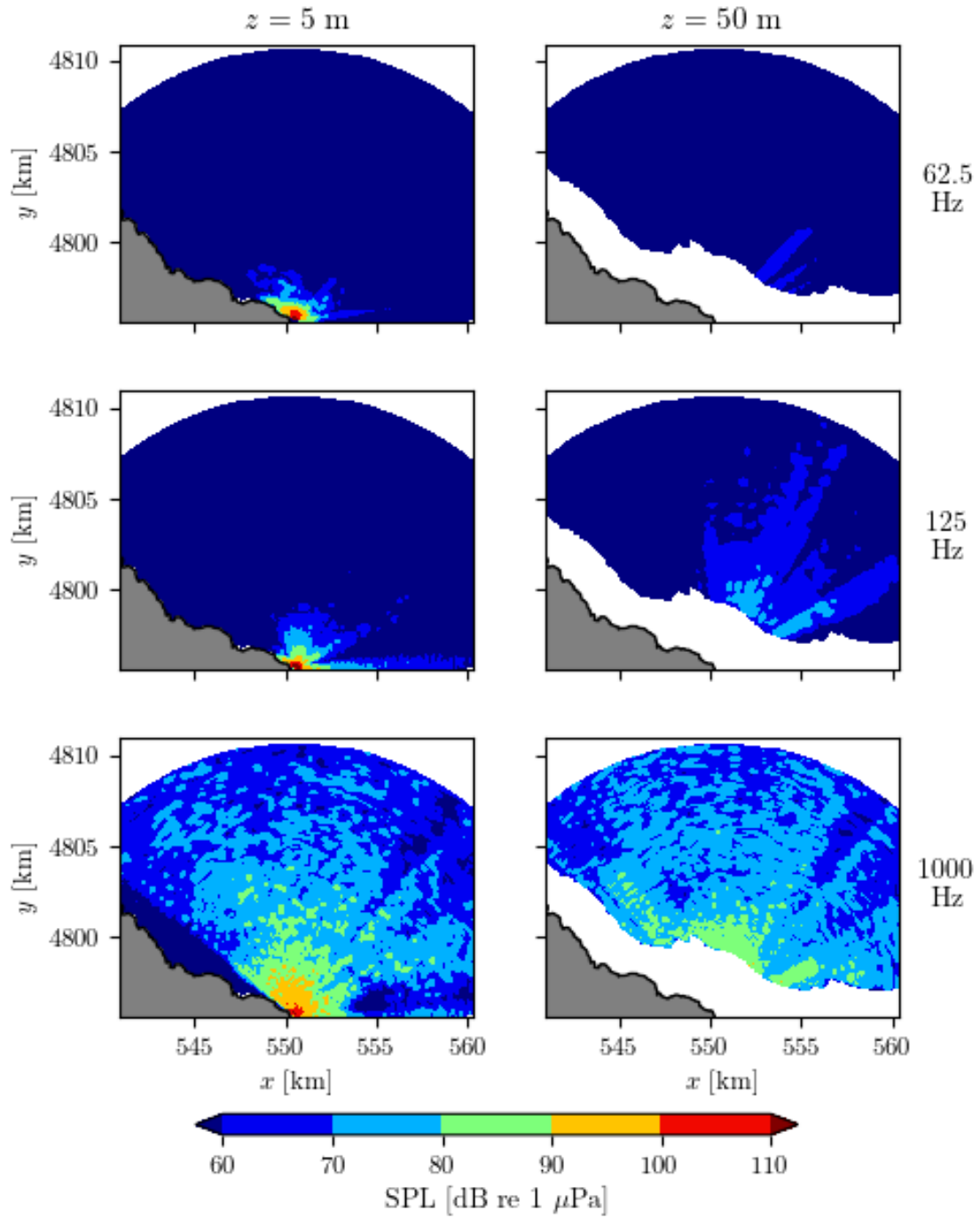


Figure 39. SPL maps  $1 \leq H_w < 2$  m in the Mutriku scenario.

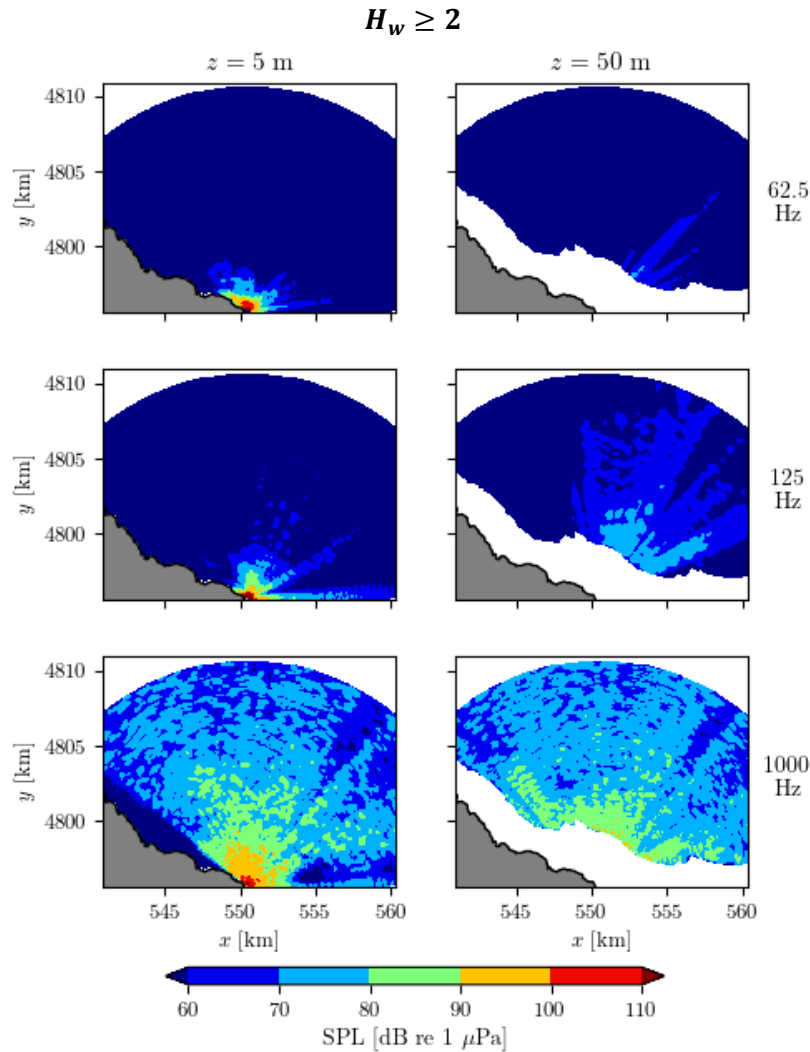


Figure 40. SPL maps for  $H_w \geq 2$  m in the Mutriku scenario.

From these results it is clear that at the lower frequencies, even if the source levels are higher at them, the SPL reach low levels at distances as close as 1 km from the source, because of the cut-off filter phenomena.

In the other hand, for the average (in depth) sound pressure level fields (case 1), the results are shown in Figure 41 (now with further zoom in the device location), along with the isoacoustic curves corresponding to the respective  $SPL_{off}$  values in each case. Here, the disturbance distance seems higher, however, we have to recall that this is simply the case because the source level might be overestimated.

Similarly, in the Figure 42, the fields are displayed for the depths in which the average SPL is maximum (case 2); in this case, 40, 40, 30 metres. Note again that, since the maximum average SPL distribution is found for 40 and 50 metres depth, the near field acoustic field is non-existent because of the very shallow environment in the Mutriku beach.

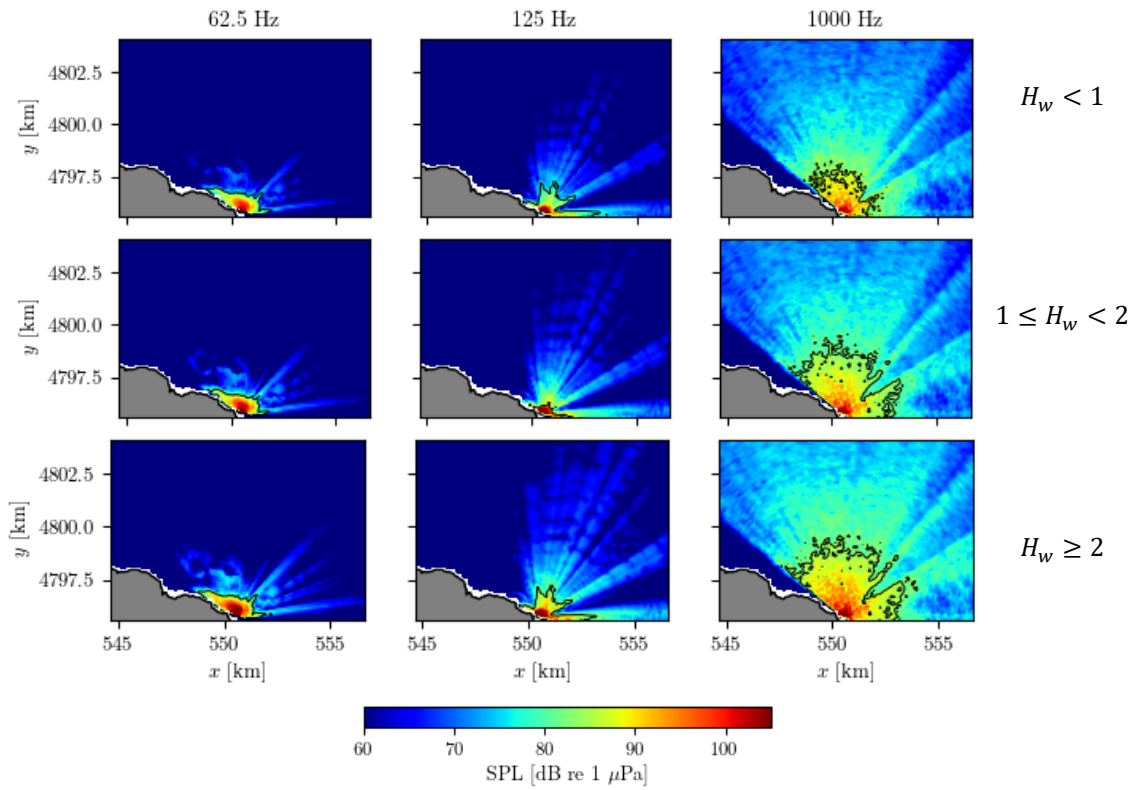


Figure 41. Average (in depth) SPL for the Mutriku scenario.

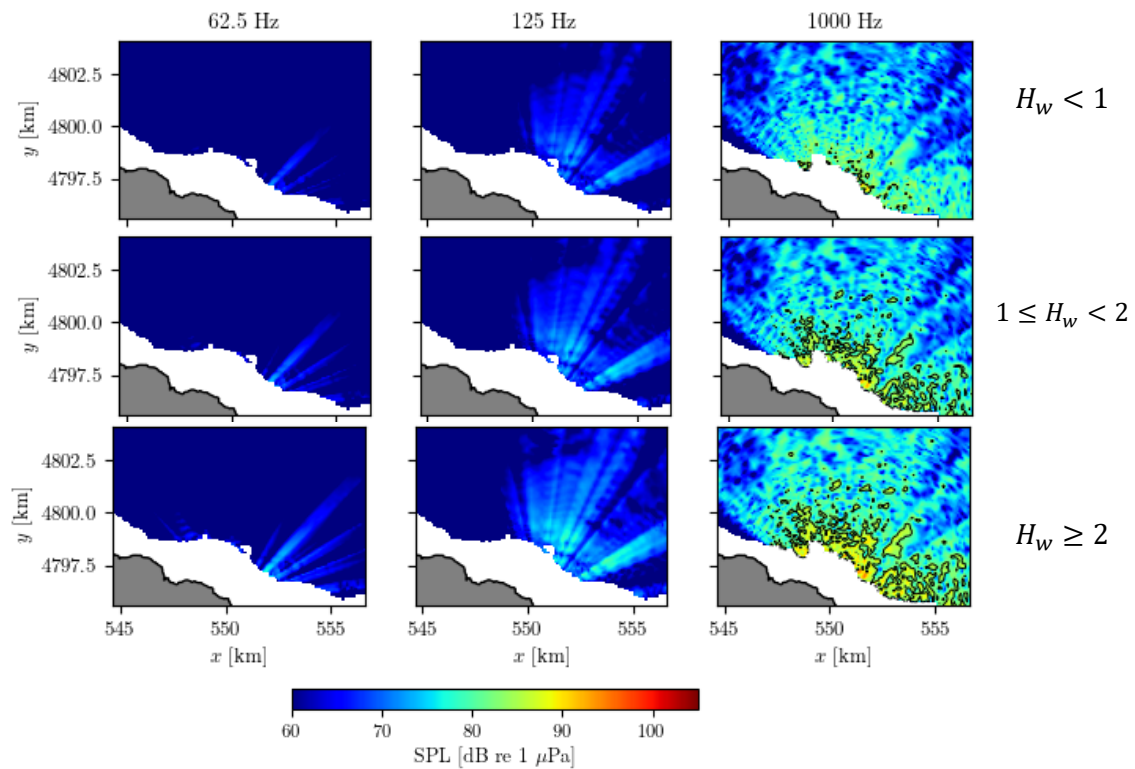
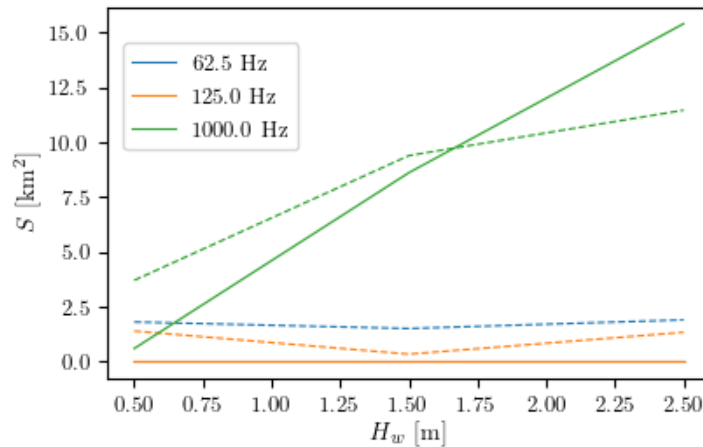


Figure 42. SPL maps for the depths with highest average SPL value in the case of Mutriku (40, 50, and 50 m from left to right).

### 5.3.2.2 Metrics

First, let us find the isocurve defined by the equality  $SPL = SPL_{off}$ , in two cases, as was performed in the MARMOK-A-5 case. In the first one, we use the averaged in depth SPL field; in the second one, we take the depth in which the average SPL (in the polar plane) is highest.

Then, we calculate both the mean distance from the source of these iso-acoustic curves and the area of such (closed) contours. The results are shown in the Figure 43. We see the higher values of disturbance for the 1000 Hz frequency in both cases.



**Figure 43.** Total surface area of the iso-acoustic closed contour curves for the case of Mutriku. In dashed lines, the case 1 (z-mean TL); in solid lines, the case 2 (min TL).

Another metric of interest is the dependence of SPL with radial distance. In this sense, in the following figure (**Figure 44**), the average value in depth of these values (for every frequency and wave height bin) has been computed and shown, as well as the baseline background noise levels (as dotted lines).

For the case 2 (using those z planes in which the average TL is minimum) we refer to **Figure 45**, against the corresponding background levels for such frequencies and wave heights.

The exact distances at which both regimen levels are equal are displayed in **Table 18**. These distances are simply obtained by finding the intersection between the dashed and solid lines in the previous plots. As the case 2 does not allow a well-behaved diverging field from the device, we omit its corresponding table.

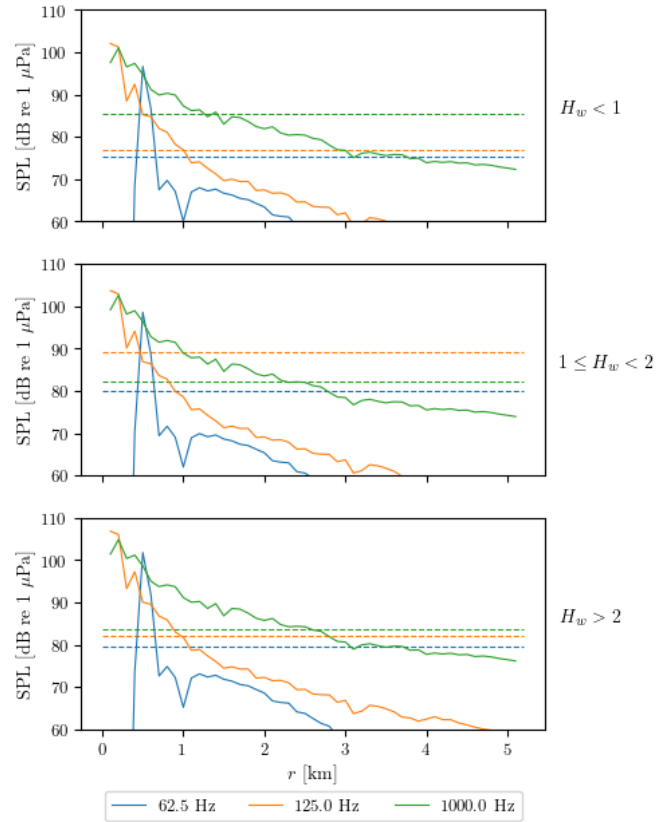


**Figure 44.** Average value in depth of SPL (case 1) sampled in concentric annuli around the Mutriku power plant (solid) with corresponding  $SPL_{off}$  (dashed).

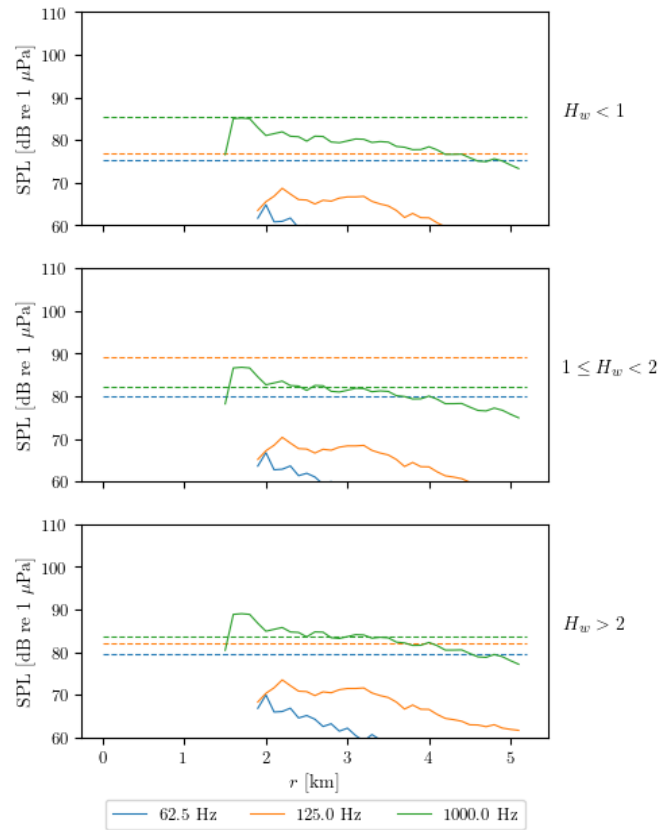


**Figure 45.** SPL (case 2) sampled in concentric annuli around the Mutriku power plant (solid) with corresponding  $SPL_{off}$  (dashed).

**Table 18.** Distances (m) from the device at which the mean of the depth-averaged SPL field drops below  $SPL_{off}$ , for the Mutriku case.

$H_w$	$f$ [Hz]		
	62.5	125	1000
[0,1)	659.6	1001.6	1261.4
[1,2)	644.4	467.6	2244.3
[2,5)	664.0	969.7	2593.7

## 6. Conclusions

In this deliverable, the main results from the work done in the acoustic modelling of the several devices studied in this project has been presented.

- **MARMOK-A-5:**
  - This device sound emission is most energetic in the 62.5 Hz band, although worse acoustic propagation conditions exist for this case, as the shallow water environment inhibits efficient sound transmission. When considering the depth in which greater values of SPL are found, the area of disturbance (for which  $SPL_{on} > SPL_{off}$ ) obtained is  $0.9 \text{ km}^2$  for such frequency and wave heights between 0 and 1 metre, which is equivalent to a 0.28 km radius circle around the device.
  - When considering a swarm of 80 identic devices, differences up to a maximum of 50 dB re  $1 \text{ } \mu\text{Pa}$  are found between this and the single device scenario (placed in the centre of the swarm), for the incoherent case. The radial distances (from the centre of the swarm) at which the sound pressure level fields are indistinguishable from the background noise levels are now much greater though, with maximum values for low wave heights (where there is less background noise) and frequencies around 3.4 km.
- **Mutriku:**
  - The highest acoustic disturbances are found in the 1 kHz band, with maximum values SPL around 110 dB re  $\mu\text{Pa}$ . When considering the depth in which greater values of SPL are found, the area of disturbance obtained is  $15 \text{ km}^2$ , for such frequency and wave heights greater than 2 meters. In addition, for the depth-averaged SPL field, the maximum distance at which  $SPL_{on} > SPL_{off}$  is satisfied is 2593.7 meters from the plant.
  - It must be noted (from D2.3) that the uncertainty in the source level values is around the calculated difference in SPL.

## 7. References

- [1] G. W. Boehlert y A. B. Gill, «Environmental and ecological effects of ocean renewable energy development - A current synthesis,» *Oceanography*, pp. 68-81, 2010.
- [2] L. S. Weilgart, «The impacts of anthropogenic ocean noise on cetaceans and implications for management,» *Canadian Journal of Zoology*, pp. 1091-1116, 2007.
- [3] M. Melikoglu, «Current status and future of ocean energy sources: a global review,» *Ocean Engineering*, pp. 563-573, 2018.
- [4] N. Khan, A. Kalair, N. Abas y A. Haider, «Review of ocean tidal, wave and thermal energy technologies,» *Renewable and Sustainable Energy Reviews*, pp. 590-604, 2017.
- [5] P. A. Vinagre, E. Cruz, P. Chainho, P. Ruiz, I. Felis, I. Muxika y J. Bald, «Deliverable 2.1 Monitoring plans for Noise, Electromagnetic Fields and Seabed Integrity. Corporate deliverable of the Wave Energy in the Southern Europe (WESE),» 2019.
- [6] I. Felis, E. Madrid y R. Álvarez-Castellanos, «Deliverable 2.3 Acoustic Monitoring. Corporate deliverable of the WESE Project funded by the European Commission,» 2020.
- [7] R. Dekeling, M. L. Tasker, A. J. Van der Graaf, M. A. Ainslie, M. H. Andersson, M. André, J. F. Borsani, K. Brensing, M. Castellote, D. Cronin, D. Dalen, T. Folegot, T. Leaper, J. Pajala, P. Redman, S. P. Robinson, P. Sigray y Sutton, «Monitoring Guidance for Underwater Noise in European Seas, Part II,» Publications Office of the European Union, Luxembourg, 2014.
- [8] L. Wang, K. Heany, T. Pangerc, P. Theobald, S. Robinson y M. Ainslie, «Review of underwater acoustic propagation models,» 2014.
- [9] K. V. Mackenzie, «Nine-term equation for sound speed in the oceans,» *The Journal of the Acoustical Society of America*, 1981.

- [10] X. Lurton, *An Introduction to Underwater Acoustics: Principles and Applications*, Springer, 2002.
- [11] R. J. Urick, *Principles of underwater sound*, 3 ed., California: McGraw-Hill, 1983.
- [12] K. B. Smith, «Convergence, stability, and variability of shallow water acoustic predictions using a split-step Fourier Parabolic Equation Model,» *Journal of Computational Acoustics*, vol. 9, n° 1, pp. 243-285, 2001.
- [13] J. Bald, A. Uriarte, P. Ruiz, P. Cervantes y N. Ortega, «Acoustic characterization of Mutriku OWC Plant,» de *III Marine Energy Week*, Bilbao, 2017.